

# Whole Brain Susceptibility Mapping Using Harmonic Incompatibility Removal\*

Chenglong Bao<sup>†</sup>, Jae Kyu Choi<sup>‡</sup>, and Bin Dong<sup>§</sup>

**Abstract.** Quantitative susceptibility mapping (QSM) uses the phase data in magnetic resonance signal to visualize a three dimensional susceptibility distribution by solving the magnetic field to susceptibility inverse problem. Due to the presence of zeros of the integration kernel in the frequency domain, QSM is an ill-posed inverse problem. Although numerous regularization based models have been proposed to overcome this problem, the incompatibility in the field data has not received enough attention, which leads to deterioration of the recovery. In this paper, we show that the data acquisition process of QSM inherently generates a harmonic incompatibility in the measured local field. Based on such discovery, we propose a novel regularization based susceptibility reconstruction model with an additional sparsity based regularization term on the harmonic incompatibility. Numerical experiments show that the proposed method achieves better performance than the existing approaches.

**Key words.** Quantitative susceptibility mapping, magnetic resonance imaging, deconvolution, partial differential equation, harmonic incompatibility removal, (tight) wavelet frames, two system regularization

**AMS subject classifications.** 35R30, 42B20, 45E10, 65K10, 68U10, 90C90, 92C55

**1. Introduction.** Quantitative susceptibility mapping (QSM) is a novel imaging technique that visualizes the magnetic susceptibility distribution from the measured field data associated with magnetization  $\mathbf{M} = (M_1, M_2, M_3)$  induced in the body by an MR scanner. The magnetic susceptibility  $\chi$  is an intrinsic property of the material which relates  $\mathbf{M}$  and the magnetic field  $\mathbf{H} = (H_1, H_2, H_3)$  through  $\mathbf{M} = \chi \mathbf{H}$  [49]. As physiological and/or pathological processes alter tissues' magnetic susceptibilities, QSM has been widely applied in biomedical image analysis [49]. Applications include demyelination, inflammation, and iron overload in multiple sclerosis [10], neurodegeneration and iron overload in Alzheimer's disease [1], Huntington's disease [55], changes in metabolic oxygen consumption [26], hemorrhage including microhemorrhage and blood degradation [30], bone mineralization [16], drug delivery using magnetic nanocarriers [38], etc.

QSM uses the phase data of a complex gradient echo (GRE) signal as the phase linearly increases with respect to the field perturbation induced by the magnetic susceptibility distribution in an MR scanner [57]. More concretely, assume that an object is placed in an MR scanner with the main static magnetic field  $\mathbf{B}_0 = (0, 0, B_0)$  where  $B_0$  is a positive constant. Then, for any  $\mathbf{x} \in \mathbb{R}^3$ , the observed complex GRE signal  $I(\mathbf{x}, TE)$  at an echo time  $TE$  sec is

\*Submitted to the editors DATE.

**Funding:** The research of the second author is partially supported by General Financial Grant from the China Postdoctoral Science Foundation (No. 2017M611539). The research of the third author is supported by NSFC grant 91530321.

<sup>†</sup>Yau Mathematical Sciences Center, Tsinghua University, Beijing, 100084 China, (clbao@math.tsinghua.edu.cn).

<sup>‡</sup>Corresponding Author. Institute of Natural Sciences, Shanghai Jiao Tong University, Shanghai, 200240 China, (jaycj@sjtu.edu.cn).

<sup>§</sup>Beijing International Center for Mathematical Research, Peking University, Beijing, 100871 China, (dongbin@math.pku.edu.cn).

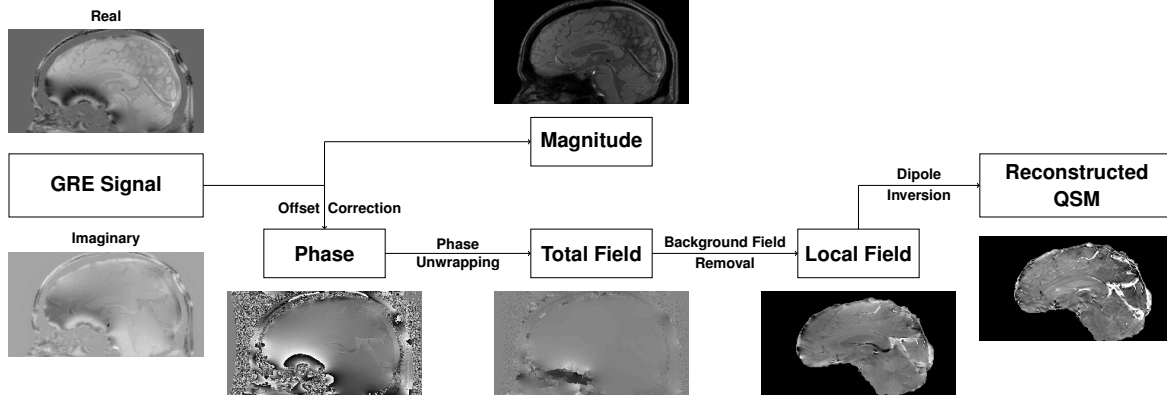


**Figure 1.** Schematic diagram of QSM reconstruction process.

modeled as

$$I(\mathbf{x}, TE) = m(\mathbf{x}) \exp \{ -i(b(\mathbf{x})\omega_0 B_0 TE + \theta_0(\mathbf{x})) \}, \quad (1.1)$$

where  $\omega_0 = 42.577\text{MHz/T}$  is the proton gyromagnetic ratio,  $b$  is the total field induced by the susceptibility distribution in an MR scanner, and  $\theta_0$  is the coil sensitivity dependent phase offset. The magnitude image  $m(\mathbf{x})$  in (1.1) is proportional to the proton density [57], and the phase  $\theta(\mathbf{x})$  in  $I(\mathbf{x}, TE)$  is written as

$$\theta(\mathbf{x}) = b(\mathbf{x})\omega_0 B_0 TE + \theta_0(\mathbf{x}). \quad (1.2)$$

Based on the observations  $\theta(\mathbf{x})$ , QSM aims at visualizing the susceptibility distribution  $\chi(\mathbf{x})$  in the region of interests (ROI)  $\Omega$  which occupies the water and brain tissues. Note that the ROI  $\Omega$  can be readily determined by  $I(\mathbf{x}, TE)$  (and thus by  $m(\mathbf{x})$ ) as  $m(\mathbf{x}) = |I(\mathbf{x}, TE)| \approx 0$  whenever  $\mathbf{x} \notin \Omega$  [34, 46, 57]. The standard QSM consists of the following four steps: offset correction, phase unwrapping, background field removal and dipole inversion (see Figure 1 for the overview of the process). The first three steps extract the local field  $b_l$  that is contained in the total field  $b$ : the offset correction removes/corrects  $\theta_0(\mathbf{x})$  from  $\theta(\mathbf{x})$  to obtain  $b(\mathbf{x})\omega_0 B_0 TE$  (the offset corrected phase) lying in  $(-\pi, \pi]$ ; the phase unwrapping removes the artificial jumps in the offset corrected phase when estimating the total field  $b$ ; the background field removal eliminates the field induced by the susceptibility outside  $\Omega$  such as skulls and nasal cavity. Interested readers may refer to [34, 35, 45, 46, 57, 61] for more details.

Given the local field  $b_l$ , the dipole inversion recovers the susceptibility distribution  $\chi$  in  $\Omega$  by solving the following convolution relation [35, 36, 37]:

$$b_l(\mathbf{x}) = \text{pv} \int_{\Omega} d(\mathbf{x} - \mathbf{y})\chi(\mathbf{y})d\mathbf{y}, \quad (1.3)$$

where pv denotes the principal value [53] of the singular integral with the kernel  $d$ :

$$d(\mathbf{x}) = \frac{2x_3^2 - x_1^2 - x_2^2}{4\pi|\mathbf{x}|^5}.$$

In the frequency domain, (1.3) reads

$$\mathcal{F}(b_l)(\boldsymbol{\xi}) = \mathcal{D}(\boldsymbol{\xi})\mathcal{F}(\chi)(\boldsymbol{\xi}) = \left(\frac{1}{3} - \frac{\xi_3^2}{|\boldsymbol{\xi}|^2}\right) \mathcal{F}(\chi)(\boldsymbol{\xi}) \quad (1.4)$$

where  $\mathcal{D} = \mathcal{F}(d)$  is the Fourier transform of  $d$  and  $\mathcal{D}(\mathbf{0}) = 0$  by convention [25]. From (1.4), it is easy to see that recovering the susceptibility distribution  $\chi$  is ill-posed as  $\mathcal{D}$  vanishes on the critical manifold  $\Gamma_0 = \{\boldsymbol{\xi} \in \mathbb{R}^3 : \xi_1^2 + \xi_2^2 - 2\xi_3^2 = 0\}$ . This ill-posedness leads to the streaking artifacts unless the data  $b_l$  satisfies a proper compatibility condition [12].

**1.1. Existing QSM Reconstruction Methods.** In the literature, various QSM reconstruction methods have been explored to deal with the ill-posed nature of the inverse problem (1.4). Early attempts mainly focus on the direct methods based on the modification of (1.4) near  $\Gamma_0$  [29]. One benchmark method, called the truncated K-space division (TKD) [51], finds the approximate solution to (1.4) via:

$$\chi_h = \mathcal{F}^{-1}(\mathcal{X}_h), \quad \text{where } \mathcal{X}_h(\boldsymbol{\xi}) = \frac{\text{sign}(\mathcal{D}(\boldsymbol{\xi}))}{\max\{|\mathcal{D}(\boldsymbol{\xi})|, \hbar\}} \mathcal{F}(b_l)(\boldsymbol{\xi}) \quad (1.5)$$

with a threshold level  $\hbar > 0$ . Another method recovers  $\chi$  via solving the following Tikhonov regularization [31]:

$$\min_{\chi} \frac{1}{2} \|A\chi - b_l\|_2^2 + \varepsilon \|\chi\|_2^2 \quad (1.6)$$

where  $\varepsilon > 0$  and  $A$  denotes the forward operator that is obtained by discretizing the kernel  $\mathcal{D}$ . Recently, some other direct methods are proposed, e.g. the iterative susceptibility weighted imaging and susceptibility mapping [54], the analytic continuation [40] and so on. Even though these direct methods are simple to implement, they can introduce additional artifacts due to the modification of  $1/\mathcal{D}$  near  $\Gamma_0$  in the frequency domain [12, 29, 41].

In recent years, the regularization based methods have been proposed and show the superior performance over the direct method [29, 56]. Mathematically, it is formulated as solving the minimization problem:

$$\min_{\chi} F(b_l|\chi) + R(\chi), \quad (1.7)$$

where  $F(b_l|\chi)$  denotes the data fidelity term and  $R(\chi)$  is the regularization term which mostly promotes the sparse approximation of  $\chi$  under some linear transformation such as total variation and wavelet frames. According to the choices of  $F(b_l|\chi)$ , the regularization based methods can be classified into the *integral approaches* and the *differential approaches* [29]. The most widely used integral approaches are based on the convolution relation (1.3). For example,  $F(b_l|\chi) = \frac{1}{2} \|A\chi - b_l\|_2^2$  when the data is corrupted by a white Gaussian noise. Even though the integral approach is capable of suppressing streaking artifacts, it is empirically reported in [29] that the reconstructed image can contain the shadow artifacts in the region of piecewise constant susceptibility. The differential approaches are based on the following partial differential equation (PDE)

$$-\Delta b_l(\mathbf{x}) = P(D)\chi(\mathbf{x}) = \left(-\frac{1}{3}\Delta + \frac{\partial^2}{\partial x_3^2}\right) \chi(\mathbf{x}) \quad \mathbf{x} \in \Omega \quad (1.8)$$

which is derived from the Maxwell's equation [24, 49]. In this case, one typical fidelity term is  $F(b_l|\chi) = \frac{1}{2} \|P(D)\chi + \Delta b_l\|_2^2$  by considering  $-\Delta b_l$  as a measurement. Compared with the integral approach, the differential approach is able to restore susceptibility image with less shadow artifacts. However, the noise in the data can be amplified by  $-\Delta$ , which leads to the streaking artifacts [57]. In [29], the differential approach is implemented by incorporating the spherical mean value (SMV) filter  $S_r$  with a radius  $r > 0$  [34] into the integral approach:

$$\min_{\chi} \frac{1}{2} \|S_r(A\chi - b_l)\|_2^2 + R(\chi). \quad (1.9)$$

Since the implementation of  $S_r$  causes the erosion of  $\Omega$  according to the choice of  $r$ , the loss of anatomical information near  $\partial\Omega$  is inevitable at the cost of the shadow artifact removal [29].

**1.2. Motivations and Contributions of Our Approach.** Even though the equations (1.3) and (1.8) are known to be equivalent [12, 29, 41], it is observed that the local field  $b_l$  defined as (1.3) is a particular solution to the PDE (1.8). Whenever the data acquisition is based on the PDE (1.8), the measured local field data will be written as the superposition of  $b_l$  in (1.3) and the ambiguity of  $-\Delta$ , which will be referred as the *harmonic incompatibility*. Therefore, we need to identify/remove the harmonic incompatibility from the measured local field data for better reconstruction results as it is smooth, analytic and satisfies the mean value property in an open set [21], which are different from the noise properties.

To do this, we note that the background field removal is related to the PDE (1.8) with some boundary condition as the background field  $b_b$  is harmonic in  $\Omega$  [34, 45, 57, 61]. However,  $b_l$  in (1.3) is a particular solution to (1.8) in  $\mathbb{R}^3$  (i.e. it can be represented by the fundamental solution of  $-\Delta$ ) [12] while the measured local field data obtained from the boundary value problem is represented by the Green's function associated with the boundary condition. This means that it is inevitable that the measured data contains the incompatibility associated with the imposed boundary condition. In this paper, we discover that this incompatibility is indeed harmonic except on  $\partial\Omega$  (See Theorem 2.1 for details and Figures 2 and 3 for illustrations), and thus, we can reestablish the forward model by taking the harmonic incompatibility into account.

Based on this discovery, we propose a novel regularization based susceptibility reconstruction model which will be referred as the harmonic incompatibility removal (HIRE) model. Generally, it is difficult to explicitly model this harmonic incompatibility and/or to directly impose its property into the susceptibility reconstruction model due to the complicated geometry of human brains. Motivated by the recent success of two system regularization in image restoration [5, 17, 27, 33], we additionally impose the sparse regularization of incompatibility into the original regularization based QSM model since the Laplacian of the incompatibility is mostly supported near  $\partial\Omega$ . Note that the harmonic incompatibility is derived mathematically which is different from the traditional two system regularization methods. Within the new model, we can suppress the incompatibility other than the noise, achieving the whole brain imaging with less artifacts together with the regularization of susceptibility image by tight wavelet frames. Experiments on both brain phantom and vivo MR data show the state-of-the-art performance of our proposed approach.

**1.3. Organization of Paper.** In [section 2](#), we introduce our HIRE model for whole brain susceptibility imaging. More precisely, we first briefly review the biophysics forward model of QSM in [subsection 2.1](#), and characterize the harmonic incompatibility in the local field data in [subsection 2.2](#). Based on the characterization, we introduce the proposed HIRE model in [subsection 2.3](#), followed by an alternating minimization algorithm in [subsection 2.4](#). In [section 3](#), we present experimental results for both brain phantom and in vivo MR data, and the concluding remarks are given in [section 4](#).

## 2. Harmonic Incompatibility Removal (HIRE) Model for Whole Brain Imaging.

**2.1. Preliminaries on Biophysics of QSM.** In an MRI scanner with the main static magnetic field  $\mathbf{B}_0 = (0, 0, B_0)$  where  $B_0$  is a positive constant, objects gain a magnetization  $\mathbf{M}(\mathbf{x})$ . This magnetization generates a macroscopic field  $\mathbf{B}(\mathbf{x})$  satisfying the following magnetostatic Maxwell's equation [\[24, 49\]](#)

$$\begin{aligned}\nabla \cdot \mathbf{B} &= 0 \\ \nabla \times \mathbf{B} &= \mu_0 \nabla \times \mathbf{M},\end{aligned}\tag{2.1}$$

where  $\mu_0 = 8.854 \times 10^{-12} \text{F/m}$  is the vacuum permittivity. Since the MRI signal is generated by the microscopic field  $\mathbf{B}_\ell(\mathbf{x})$  experienced by the spins of water protons [\[29\]](#), we use the following Lorenz sphere correction model [\[24\]](#):

$$\mathbf{B}_\ell(\mathbf{x}) = \mathbf{B}(\mathbf{x}) - \frac{2}{3}\mu_0 \mathbf{M}(\mathbf{x})\tag{2.2}$$

to relate  $\mathbf{B}(\mathbf{x})$  and  $\mathbf{B}_\ell(\mathbf{x})$ .

Note that since  $\mathbf{M}(\mathbf{x})$  is generated by  $\mathbf{B}_0$  field, we have  $\mathbf{M}(\mathbf{x}) = (0, 0, M(\mathbf{x}))$ . Moreover, since we consider the linear magnetic materials with  $|\chi| \ll 1$ ,  $\chi$  can be approximated as

$$\chi(\mathbf{x}) \approx \frac{\mu_0}{B_0} M(\mathbf{x}).\tag{2.3}$$

Finally, we introduce the total field  $b(\mathbf{x})$  as

$$b(\mathbf{x}) = \frac{B_{\ell 3}(\mathbf{x}) - B_0}{B_0}\tag{2.4}$$

where  $B_{\ell 3}(\mathbf{x})$  denotes the third component of  $\mathbf{B}_\ell(\mathbf{x})$ .

Combining [\(2.1\)–\(2.4\)](#) and taking the third component into account only, we obtain the following relation between  $\chi$  and  $b$  in the frequency domain:

$$|\boldsymbol{\xi}|^2 \mathcal{F}(b)(\boldsymbol{\xi}) = \left( \frac{1}{3} |\boldsymbol{\xi}|^2 - \xi_3^2 \right) \mathcal{F}(\chi)(\boldsymbol{\xi}),\tag{2.5}$$

which gives

$$-\Delta b = P(D)\chi := \left( -\frac{1}{3}\Delta + \frac{\partial^2}{\partial x_3^2} \right) \chi.\tag{2.6}$$

Then for a given susceptibility distribution  $\chi$  (in  $\mathbb{R}^3$ ), the general solution  $b$  which is bounded everywhere in  $\mathbb{R}^3$  is expressed as

$$b(\mathbf{x}) = \int_{\mathbb{R}^3} \Phi(\mathbf{x} - \mathbf{y}) \left( -\frac{1}{3} \Delta_{\mathbf{y}} + \frac{\partial^2}{\partial y_3^2} \right) \chi(\mathbf{y}) d\mathbf{y} + b_0 \quad (2.7)$$

where  $b_0$  is some constant, and  $\Phi(\mathbf{x}) = 1/(4\pi|\mathbf{x}|)$ .

In MRI, the phase of a complex GRE MR signal is linear with respect to the total field  $b$  in (2.7) (e.g. [57]), and the constant  $b_0$  is determined by the coil sensitivity of an MR scanner as the coil sensitivity dependent phase offset is in general assumed to be a constant [25, 46]. However, since we can remove it during the phase estimation from the multi echo GRE signal [15, 31, 39], we assume that  $b_0 = 0$  and

$$b(\mathbf{x}) = \int_{\mathbb{R}^3} \Phi(\mathbf{x} - \mathbf{y}) \left( -\frac{1}{3} \Delta_{\mathbf{y}} + \frac{\partial^2}{\partial y_3^2} \right) \chi(\mathbf{y}) d\mathbf{y} \quad (2.8)$$

in the rest of this paper. Note that  $b$  defined as above is induced by the susceptibility distribution *in the entire space*, which is different from  $b_l$  in (1.3).

**Remark 2.1.** Since [12, Proposition A.1.] has discussed the equivalence between (2.8) and the following representation in the literature

$$b(\mathbf{x}) = \text{pv} \int_{\mathbb{R}^3} d(\mathbf{x} - \mathbf{y}) \chi(\mathbf{y}) d\mathbf{y}, \quad (2.9)$$

we shall use (2.8) in the rest of this paper. Note that (2.8) avoids the singularity of the kernel  $d(\mathbf{x} - \mathbf{y})$  in (2.9) as  $\Phi(\mathbf{x} - \mathbf{y})$  is locally integrable near  $\mathbf{x} = \mathbf{y}$ .

**2.2. Characterization of Harmonic Incompatibility in Local Field Data.** In QSM, the total field  $b(\mathbf{x})$  is obtained from the phase data of a complex GRE MR signal [46, 57]. However, since the GRE signal is not available outside  $\Omega$ , the information of  $b$  is available only inside  $\Omega$ . Moreover, even if  $\chi$  is compactly supported, the support of  $b$  may not necessarily coincide with that of  $\chi$ , which inevitably leads to the information loss outside  $\Omega$  [34, 46, 57].

Since the total field  $b$  depends on the susceptibility distribution *throughout the entire space* [46], it consists of the background field  $b_b$  induced from the susceptibility outside  $\Omega$ , which is of no interest, and the local field  $b_l$  by the susceptibility in  $\Omega$  which we aim to visualize. Since the substantial susceptibility sources are usually located outside  $\Omega$  which makes the background field  $b_b$  dominant in  $b$  compared to the local field  $b_l$ , we need to remove the background field from the (incomplete) total field prior to the dipole inversion [34, 35, 45, 46, 57, 61].

In the literature, given that the background field is harmonic in  $\Omega$  [34, 45, 57, 61], the background field removal methods take the form of the following Poisson's equation in [61]:

$$\begin{cases} -\Delta b_m = -\Delta b & \text{in } \Omega \\ b_m = 0 & \text{on } \partial\Omega \end{cases} \quad (2.10)$$

where the subscript  $m$  is used to tell the “measured” local field  $b_m$  from the true local field  $b_l$ . Under this setting, we present **Theorem 2.1** which characterizes the relation between (2.10)

and the PDE (2.6), and the discrepancy between the measured local field  $b_m$  obtained by (2.10) and the true local field  $b_l$ , i.e. the incompatibility in  $b_m$ . More precisely, the boundary value problem (2.10) solves (2.6) with the same boundary condition ( $b_m = 0$  on  $\partial\Omega$ ), and its solution  $b_m$  contains a harmonic incompatibility associated with the boundary condition of (2.10). (See Figures 2 and 3 for illustrations.)

**Theorem 2.1.** *Let  $\Omega \subseteq \mathbb{R}^3$  be an open and bounded set with  $C^1$  boundary  $\partial\Omega$ . Assume that the total field  $b = b_l + b_b$  satisfies (2.8) for a given susceptibility  $\chi$ . Let  $b_m : \bar{\Omega} \rightarrow \mathbb{R}$  denote the measured local field obtained from the Poisson's equation (2.10). Then we have the followings:*

1.  $b_m$  solves the following boundary value problem:

$$\begin{cases} -\Delta b_m = P(D)\chi & \text{in } \Omega \\ b_m = 0 & \text{on } \partial\Omega. \end{cases} \quad (2.11)$$

2. If we extend  $b_m$  into  $\mathbb{R}^3$  by assigning  $b_m(\mathbf{x}) = 0$  for  $\mathbf{x} \notin \Omega$ , then there exists a function  $v$  such that

$$b_m(\mathbf{x}) = \int_{\Omega} \Phi(\mathbf{x} - \mathbf{y}) \left( -\frac{1}{3}\Delta_{\mathbf{y}} + \frac{\partial^2}{\partial y_3^2} \right) \chi(\mathbf{y}) d\mathbf{y} + v(\mathbf{x}) \quad (2.12)$$

for  $\mathbf{x} \in \mathbb{R}^3$ . Moreover,  $-\Delta v = 0$  except on  $\partial\Omega$ .

*Proof.* From (2.8), we can see that  $b_l$  and  $b_b$  is represented as

$$b_l(\mathbf{x}) = \int_{\Omega} \Phi(\mathbf{x} - \mathbf{y}) \left( -\frac{1}{3}\Delta_{\mathbf{y}} + \frac{\partial^2}{\partial y_3^2} \right) \chi(\mathbf{y}) d\mathbf{y} \quad (2.13)$$

$$b_b(\mathbf{x}) = \int_{\mathbb{R}^3 \setminus \Omega} \Phi(\mathbf{x} - \mathbf{y}) \left( -\frac{1}{3}\Delta_{\mathbf{y}} + \frac{\partial^2}{\partial y_3^2} \right) \chi(\mathbf{y}) d\mathbf{y} \quad (2.14)$$

respectively. Then since  $-\Delta\Phi = \delta$  (in the sense of distribution), the direct computation shows that

$$-\Delta b_l = \begin{cases} P(D)\chi & \text{in } \Omega \\ 0 & \text{in } \mathbb{R}^3 \setminus \bar{\Omega}, \end{cases} \quad \text{and} \quad -\Delta b_b = \begin{cases} 0 & \text{in } \Omega \\ P(D)\chi & \text{in } \mathbb{R}^3 \setminus \bar{\Omega}, \end{cases} \quad (2.15)$$

respectively. In other words, the governing equation in (2.10) is

$$-\Delta b_m = -\Delta b = -\Delta(b_l + b_b) = -\Delta b_l = P(D)\chi \quad \text{in } \Omega,$$

which proves 1.

For 2, let  $G(\mathbf{x}, \mathbf{y})$  denote the Green's function in  $\Omega$ :

$$G(\mathbf{x}, \mathbf{y}) = \Phi(\mathbf{y} - \mathbf{x}) - H(\mathbf{x}, \mathbf{y})$$

where for each  $\mathbf{x} \in \Omega$ , the corrector function  $H(\mathbf{x}, \mathbf{y})$  satisfies

$$\begin{cases} -\Delta_{\mathbf{y}} H(\mathbf{x}, \mathbf{y}) = 0 & \text{if } \mathbf{y} \in \Omega \\ H(\mathbf{x}, \mathbf{y}) = \Phi(\mathbf{y} - \mathbf{x}) & \text{if } \mathbf{y} \in \partial\Omega. \end{cases}$$



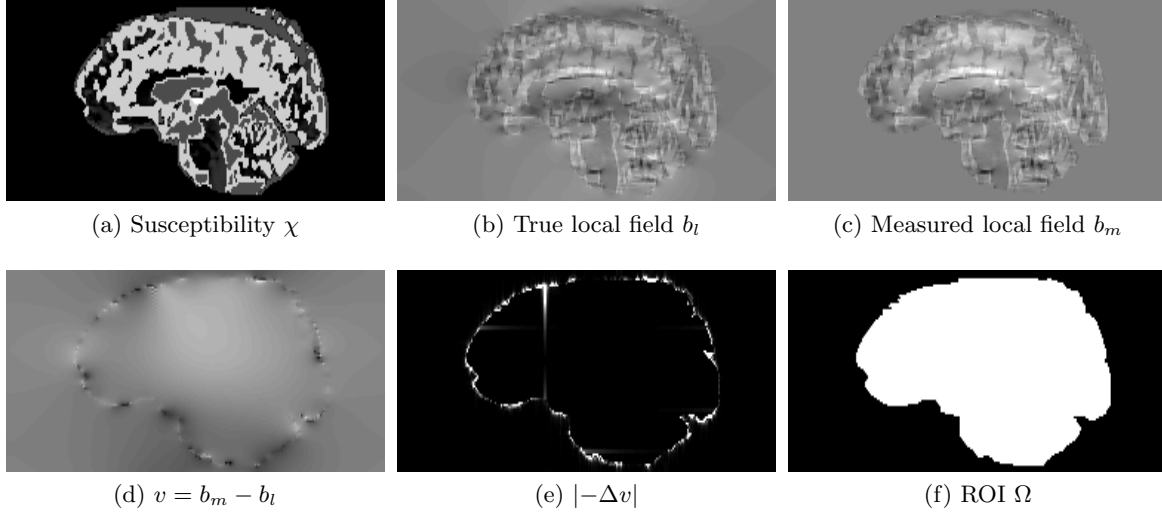


**Figure 2.** Sagittal slice images which illustrate [Theorem 2.1](#). Images of  $b_l$  and  $b_m$  are displayed in the window level  $[-0.05, 0.05]$ ,  $v$  in the window level  $[-0.025, 0.025]$ , and  $|\Delta v|$  in the window level  $[0, 0.01]$  respectively. We can see that  $-\Delta v$  is close to 0 except on  $\partial\Omega$ .

Then the solution to [\(2.10\)](#) is represented as

$$\begin{aligned} b_m(\mathbf{x}) &= \int_{\Omega} G(\mathbf{x}, \mathbf{y}) \left( -\frac{1}{3} \Delta_{\mathbf{y}} + \frac{\partial^2}{\partial y_3^2} \right) \chi(\mathbf{y}) d\mathbf{y} \\ &= \int_{\Omega} \Phi(\mathbf{x} - \mathbf{y}) \left( -\frac{1}{3} \Delta_{\mathbf{y}} + \frac{\partial^2}{\partial y_3^2} \right) \chi(\mathbf{y}) d\mathbf{y} + \mathcal{H}(\mathbf{x}) \end{aligned}$$

where we have used the fact that  $\Phi(\mathbf{y} - \mathbf{x}) = \Phi(\mathbf{x} - \mathbf{y})$ , and  $\mathcal{H}(\mathbf{x})$  is defined as

$$\mathcal{H}(\mathbf{x}) = - \int_{\Omega} H(\mathbf{x}, \mathbf{y}) \left( -\frac{1}{3} \Delta_{\mathbf{y}} + \frac{\partial^2}{\partial y_3^2} \right) \chi(\mathbf{y}) d\mathbf{y} \quad (2.16)$$

for  $\mathbf{x} \in \Omega$ .

Based on the fact that  $b_m(\mathbf{x}) = 0$  for  $\mathbf{x} \in \mathbb{R}^3 \setminus \overline{\Omega}$ , we define  $v(\mathbf{x})$  by

$$v(\mathbf{x}) = \begin{cases} \mathcal{H}(\mathbf{x}) & \text{if } \mathbf{x} \in \Omega \\ -b_l(\mathbf{x}) & \text{if } \mathbf{x} \notin \Omega. \end{cases}$$

Hence, we have

$$b_m(\mathbf{x}) = \int_{\Omega} \Phi(\mathbf{x} - \mathbf{y}) \left( -\frac{1}{3} \Delta_{\mathbf{y}} + \frac{\partial^2}{\partial y_3^2} \right) \chi(\mathbf{y}) d\mathbf{y} + v(\mathbf{x})$$

for  $\mathbf{x} \in \mathbb{R}^3$ . Finally, since  $-\Delta \mathcal{H} = 0$  in  $\Omega$ , together with [\(2.15\)](#), we have  $-\Delta v = 0$  except on  $\partial\Omega$ . This completes the proof. ■



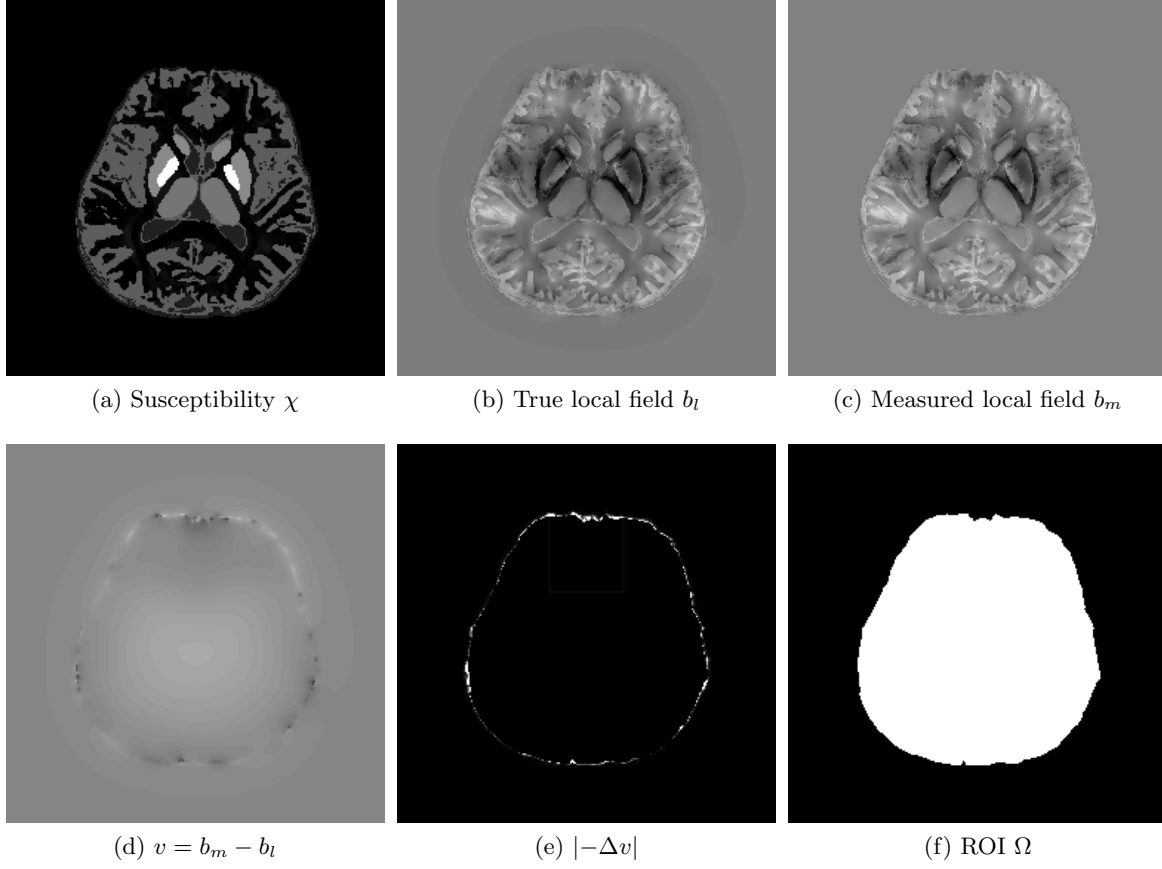


**Figure 3.** Axial slice images which illustrate *Theorem 2.1*. As in *Figure 2*, images of  $b_l$  and  $b_m$  are displayed in the window level  $[-0.05, 0.05]$ ,  $v$  in the window level  $[-0.025, 0.025]$ , and  $|\Delta v|$  in the window level  $[0, 0.01]$  respectively. We can also see that  $-\Delta v$  is close to 0 except on  $\partial\Omega$ .

**Remark 2.2.** From the proof of *Theorem 2.1*, we can observe that the harmonic incompatibility  $v$  is related to the susceptibility distribution in  $\Omega$  as well. More precisely, the standard arguments in the Green's function (e.g. [21, 48]) tell us that  $\mathcal{H}$  in (2.16) is generated by folding the information of  $b_l$  in  $\mathbb{R}^3 \setminus \bar{\Omega}$  into  $\Omega$  appropriately so that the zero boundary condition is matched. However, since the boundary of ROI, i.e. the human brain, has a complex geometry, it is in general difficult to explicitly model  $v$  by applying the techniques of Green's function to QSM.

**2.3. Proposed HIRE Susceptibility Reconstruction Model.** We begin with introducing some notation. Let  $\mathbb{O} = \{0, \dots, N_1 - 1\} \times \{0, \dots, N_2 - 1\} \times \{0, \dots, N_3 - 1\}$  denote the set of indices of  $N_1 \times N_2 \times N_3$  grids, and let  $\Omega \subseteq \mathbb{O}$  denote the set of indices corresponding to the ROI which is readily obtained by e.g. the thresholding on the magnitude image or the FSL brain extraction tool in [52]. By  $\partial\Omega$ , we mean the set of indices where the boundary condition of (2.10) is active. Finally, the space of real valued functions defined on  $\mathbb{O}$  is denoted as  $\mathcal{I}_3 \simeq \mathbb{R}^{N_1 \times N_2 \times N_3}$ .

Let  $b_m \in \mathcal{I}_3$  be the (noisy) measured local field data obtained from (2.10), which satisfies  $b_m = 0$  in  $\mathbb{O} \setminus \Omega$ . From the viewpoint of Theorem 2.1, we can model it as

$$b_m = A\chi + v + \eta$$

where  $A = \mathcal{F}^{-1}\mathcal{D}\mathcal{F}$  is the discretization of the forward operator in (2.12). Here,  $\chi \in \mathcal{I}_3$  is the unknown true susceptibility image supported in  $\Omega$ ,  $v \in \mathcal{I}_3$  is the incompatibility satisfying

$$\mathcal{L}v = 0 \quad \text{except on } \partial\Omega \quad (2.17)$$

with the discrete Laplacian  $\mathcal{L}$ , and  $\eta$  is some additive noise which is assumed to be an i.i.d. white Gaussian noise in this paper.

Note that it is in general difficult to directly impose (2.17) due to the complicated geometry of human brain. Nevertheless, we can observe that  $\mathcal{L}v$  is mostly supported near  $\partial\Omega$ , i.e.  $\mathcal{L}v$  is sparse. In addition, motivated by the successful results on the wavelet frame based image restoration (e.g. [5, 6, 8, 9]), we assume the sparse approximation of  $\chi$  under a given wavelet transformation  $W$ , and propose our HIRE model as follows:

$$\min_{\chi, v \in \mathcal{I}_3} \frac{1}{2} \|A\chi + v - b_m\|_2^2 + \lambda \|\mathcal{L}v\|_1 + \|\gamma \cdot W\chi\|_{1,2}. \quad (2.18)$$

Here,  $\|\gamma \cdot W\chi\|_{1,2}$  is the isotropic  $\ell_1$  norm of the wavelet frame coefficients [6] defined as

$$\|\gamma \cdot W\chi\|_{1,2} := \sum_{\mathbf{k} \in \mathbb{O}} \sum_{l=0}^{L-1} \gamma_l[\mathbf{k}] \left( \sum_{\alpha \in \mathbb{B}} |(W_{l,\alpha}\chi)[\mathbf{k}]|^2 \right)^{1/2}. \quad (2.19)$$

(See Appendix A for the brief introduction on the wavelet frames.)

**Remark 2.3.** If  $v \equiv 0$ , our model reduces to the integral approach model:

$$\min_{\chi \in \mathcal{I}_3} \frac{1}{2} \|A\chi - b_m\|_2^2 + \|\gamma \cdot W\chi\|_{1,2}. \quad (2.20)$$

In addition, if we fix  $v = b_m - A\chi$ , our model reduces to the  $\ell_1$  fidelity version of the following differential approach model:

$$\min_{\chi \in \mathcal{I}_3} \frac{1}{2} \|\mathcal{L}b_m - \mathcal{L}A\chi\|_1 + \|\gamma \cdot W\chi\|_{1,2} \quad (2.21)$$

as  $\mathcal{L}A\chi = \mathcal{L}b_m$  discretizes the PDE (2.6) in the sense of [12, Proposition A.1.].

Comparing our HIRE model (2.18) with the existing approaches-the integral approach (2.20) and the differential approach (2.21), our model considers the incompatibility  $v$  and noise separately which provides a more precise model for QSM. This is because  $b_m$  is obtained from the Poisson's equation (2.10) and it inevitably contains the harmonic incompatibility related to the imposed boundary condition, as described in Theorem 2.1. Even though more rigorous theoretical analysis is needed, we can somehow explain the effect of harmonic incompatibility in this manner; since the standard arguments on the harmonic functions (e.g. [21]) tell us that  $v$  is smooth and satisfies the mean value property except on  $\partial\Omega$ , it has slow variations on this

region. As a consequence, it mostly affects the low frequency components in  $b_m$  compared to the noise which mainly affects the high frequency components. Together with the fact that the critical manifold  $\Gamma_0$  forms a conic manifold in the frequency domain, the harmonic incompatibility  $v$  in  $b_m$  mainly leads to the loss of  $\mathcal{F}(\chi)$  in low frequency components.

As empirically observed in [29], the incompatibility in low frequency components of  $b_m$  leads to the shadow artifacts in the reconstructed image, while that in high frequency components leads to the streaking artifacts. Therefore, the simultaneous consideration on the incompatibilities in both components is crucial for better susceptibility imaging. The integral approach does not take the harmonic incompatibility in  $b_m$  into account, which may not be capable of suppressing the incompatibility in low frequency components of  $b_m$ , and leads to the shadow artifacts in the reconstructed images. The differential approach can be viewed as a preconditioned integral approach since the harmonic incompatibility in  $b_m$  has been removed in advance. However, the noise in  $b_m$  can be amplified by  $\mathcal{L}$  at the cost of harmonic incompatibility removal, which leads to the streaking artifacts propagating from the noise in final image[57]. In contrast, the HIRE model takes the form of integral approach which explicitly considers the incompatibility  $v$  other than the noise by incorporating its sparsity under  $\mathcal{L}$ . By doing so, we expect that the HIRE model can suppress both the noise (cause of streaking artifacts) and the harmonic incompatibility (cause of shadow artifacts), so that we can achieve the whole brain imaging with less artifacts.

Finally, we mention that the formulation of HIRE model is not limited to (2.18). In fact, we can use other regularization terms such as total variation (TV) [11, 44], total generalized variation [3, 4, 32], TV-wavelet [60], and weighted TV for morphological consistency [2, 28, 36, 47]. Moreover, the choice of the data fidelity term is not limited to the  $\ell_2$  norm either. For example, introducing the signal to noise ratio weight  $\Sigma$ , we can choose  $\|A\chi + v - b_m\|_{\Sigma}^2$  with  $\|\cdot\|_{\Sigma}^2 = \langle \Sigma \cdot, \cdot \rangle$  to compensate the spatially varying noise [29, 36]. We can also use the nonlinear fidelity term  $\|e^{i(A\chi+v)} - e^{ib_m}\|_{\Sigma}^2$  to further compensate the errors in phase unwrapping [29, 39]. Besides, thanks to the flexibility of the regularization based approach, the regularization term and the data fidelity term can be combined in a “plug and play” fashion depending on the applications [29]. Nonetheless, we will not discuss the details on such variants as it is beyond the scope of this paper. We will focus on the model (2.18) throughout this paper.

**2.4. Alternating Minimization Algorithm.** To solve the proposed HIRE model (2.18), we use the split Bregman algorithm [8, 23] in the framework of alternating direction method of multipliers [20]. More precisely, let  $d = W\chi$  and  $e = \mathcal{L}v$ . Then (2.18) is reformulated as the following constrained minimization model:

$$\begin{aligned} \min_{\chi, v, d, e} \quad & \frac{1}{2} \|A\chi + v - b_m\|_2^2 + \lambda \|e\|_1 + \|\gamma \cdot d\|_{1,2} \\ \text{subject to} \quad & d = W\chi, \quad e = \mathcal{L}v. \end{aligned}$$

Under this reformulation, we summarize the split Bregman algorithm for the HIRE model in Algorithm 1.

It is easy to see that each subproblem has a closed form solution. The solutions to (2.22)

**Algorithm 1** Split Bregman Algorithm for (2.18)**Initialization:**  $\chi^0, v^0, d^0, e^0, p^0, q^0$ **for**  $k = 0, 1, 2, \dots$  **do**    Update  $\chi$  and  $v$ :

$$\chi^{k+1} = \underset{\chi}{\operatorname{argmin}} \frac{1}{2} \|A\chi + v^k - b_m\|_2^2 + \frac{\beta}{2} \|W\chi - d^k + p^k\|_2^2 \quad (2.22)$$

$$v^{k+1} = \underset{v}{\operatorname{argmin}} \frac{1}{2} \|v + A\chi^{k+1} - b_m\|_2^2 + \frac{\beta}{2} \|\mathcal{L}v - e^k + q^k\|_2^2 \quad (2.23)$$

    Update  $d$  and  $e$ :

$$d^{k+1} = \underset{d}{\operatorname{argmin}} \|\gamma \cdot d\|_{1,2} + \frac{\beta}{2} \|d - W\chi^{k+1} - p^k\|_2^2 \quad (2.24)$$

$$e^{k+1} = \underset{e}{\operatorname{argmin}} \lambda \|e\|_1 + \frac{\beta}{2} \|e - \mathcal{L}v^{k+1} - q^k\|_2^2 \quad (2.25)$$

    Update  $p$  and  $q$ :

$$p^{k+1} = p^k + W\chi^{k+1} - d^{k+1} \quad (2.26)$$

$$q^{k+1} = q^k + \mathcal{L}v^{k+1} - e^{k+1} \quad (2.27)$$

**end for**

and (2.23) can be written as

$$\chi^{k+1} = (A^T A + \beta I)^{-1} [A^T (b_m - v^k) + \beta W^T (d^k - p^k)] \quad (2.28)$$

$$v^{k+1} = (I + \beta \mathcal{L}^T \mathcal{L})^{-1} [b_m - A\chi^{k+1} + \beta \mathcal{L}^T (e^k - q^k)]. \quad (2.29)$$

Since we use the periodic boundary conditions, both (2.28) and (2.29) can be easily solved by using the fast Fourier transform. In addition, the solutions to (2.24) and (2.25) can be expressed in terms of the soft thresholding:

$$d^{k+1} = \mathcal{T}_{\gamma/\beta} (W\chi^{k+1} + p^k) \quad (2.30)$$

$$e^{k+1} = \max(|\mathcal{L}v^{k+1} + q^k| - \lambda/\beta, 0) \operatorname{sign}(\mathcal{L}v^{k+1} + q^k). \quad (2.31)$$

Here,  $\mathcal{T}_\gamma$  is the isotropic soft thresholding in [6]: given  $d$  defined as

$$d = \{d_{l,\alpha} : (l, \alpha) \in (\{0, \dots, L-1\} \times \mathbb{B}) \cup \{(L-1, \mathbf{0})\}\}$$

and  $\gamma = \{\gamma_l : l = 0, 1, \dots, L-1\}$  with  $\gamma_l \geq 0$ ,  $\mathcal{T}_\gamma(d)$  is defined as

$$(\mathcal{T}_\gamma(d))_{l,\alpha}[\mathbf{k}] = \begin{cases} d_{l,\alpha}[\mathbf{k}], & (l, \alpha) = (L-1, \mathbf{0}) \\ \max(R_l[\mathbf{k}] - \gamma_l[\mathbf{k}], 0) \frac{d_{l,\alpha}[\mathbf{k}]}{R_l[\mathbf{k}]}, & (l, \alpha) \in \{0, \dots, L-1\} \times \mathbb{B} \end{cases} \quad (2.32)$$

where  $R_l[\mathbf{k}] = \left( \sum_{\alpha \in \mathbb{B}} |d_{l,\alpha}[\mathbf{k}]|^2 \right)^{1/2}$  for  $\mathbf{k} \in \mathbb{O}$ .

Finally, since our model (2.18) is convex, it can be verified that Algorithm 1 converges to the minimizer of (2.18) by following the framework of [8, Theorem 3.2.], whenever it has the unique global minimizer.

**3. Experimental Results.** In this section, we present some experimental results on brain phantom in [59] and in vivo MR data in [57], both of which are available on Cornell MRI Research Lab webpage<sup>1</sup>, to compare the HIRE model (2.18) with several existing approaches. Note, however, that the main focus of this paper is to propose a two system regularization model by identifying a harmonic incompatibility in the measured local field data rather than focusing on the noise property and/or the design of the regularization term. Hence, we choose to compare with the TKD method (1.5) in [51], the Tikhonov regularization (1.6) in [31], the integral approach model (2.20) and the differential approach model (2.21) as a proof of concept. All experiments are implemented on MATLAB R2017b running on a platform with 16GB RAM and Intel(R) Core(TM) i7-7700K at 3.60GHz with 8 cores.

In (2.18), (2.20), and (2.21), we choose  $\gamma$  as  $\gamma = \{\nu 2^{-l} : l = 0, \dots, L-1\}$  with  $\nu > 0$ , and we choose  $W$  to be the tensor product Haar framelet transform with 1 level of decomposition. In addition, we use the standard centered difference for  $\mathcal{L}$  in (2.18). The stopping criterion for Algorithm 1 are

$$\frac{\|\chi^{k+1} - \chi^k\|_2}{\|\chi^{k+1}\|_2} \leq 5 \times 10^{-4},$$

and both (2.20) and (2.21) are solved using the split Bregman algorithm presented in [8] with the same stopping criterion as above. Finally, we compute the root mean square error (RMSE), the structural similarity index map (SSIM) [58], and the high frequency error norm (HFEN) [42] of the brain phantom experimental results for the quantitative comparison of each reconstruction model.

**3.1. Experiments on Brain Phantom.** For the brain phantom experiments, we use  $256 \times 256 \times 98$  image with spatial resolution  $0.9375 \times 0.9375 \times 1.5\text{mm}^3$  to simulate the 11 equispaced multi echo GREs at 3T with  $TE$  ranging from 2.6msec to 28.6msec. We first simulate the true total field by adding four background susceptibility sources in the true susceptibility image to provide the background field. Then we generate the multi echo complex GRE signal by

$$I(\mathbf{k}, t) = m(\mathbf{k}) \exp \{ -i(b_l(\mathbf{k}) + b_b(\mathbf{k}))\omega_0 B_0 TE(t) \}, \quad \mathbf{k} \in \mathbb{O}, \text{ \& } t = 1, \dots, 11$$

with a given true magnitude image  $m$ , and the white Gaussian noise with standard deviation 0.02 is added to both real and complex part of each GRE signal. Using the simulated noisy multi echo GRE signal, we estimate the magnitude image and phase data using the method in [15], and the phase is further unwrapped by the method in [22] to obtain the noisy and incomplete total field  $b$ . Finally, we solve the Poisson's equation (2.10) using the method in [61] to obtain the noisy local field data  $b_m$ . (See Figures 4 and 5.)

---

<sup>1</sup><http://www.weill.cornell.edu/mri/pages/qsm.html>

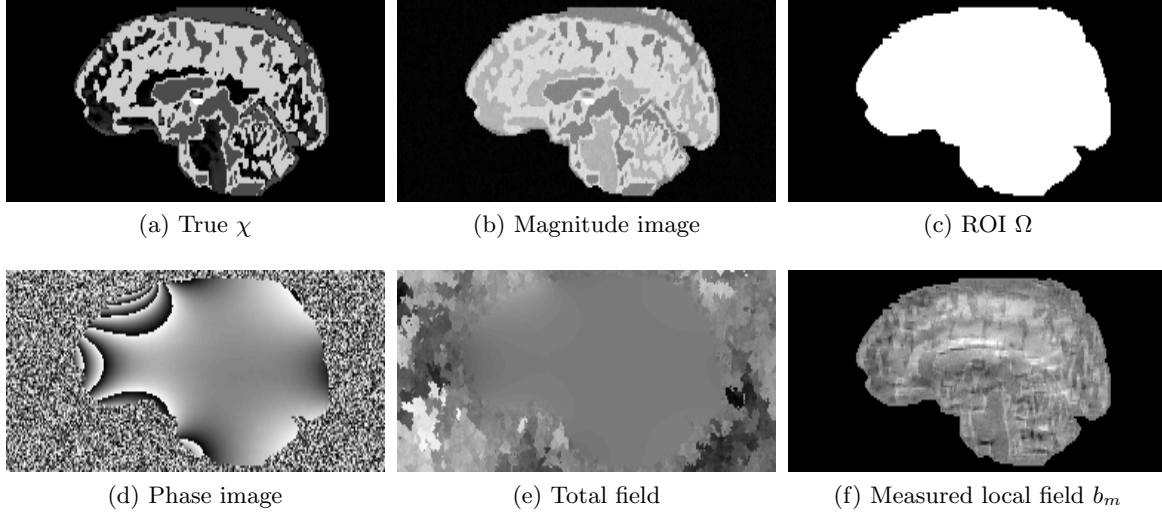


**Figure 4.** *Sagittal slice images of synthesized data sets for the brain phantom experiments.*

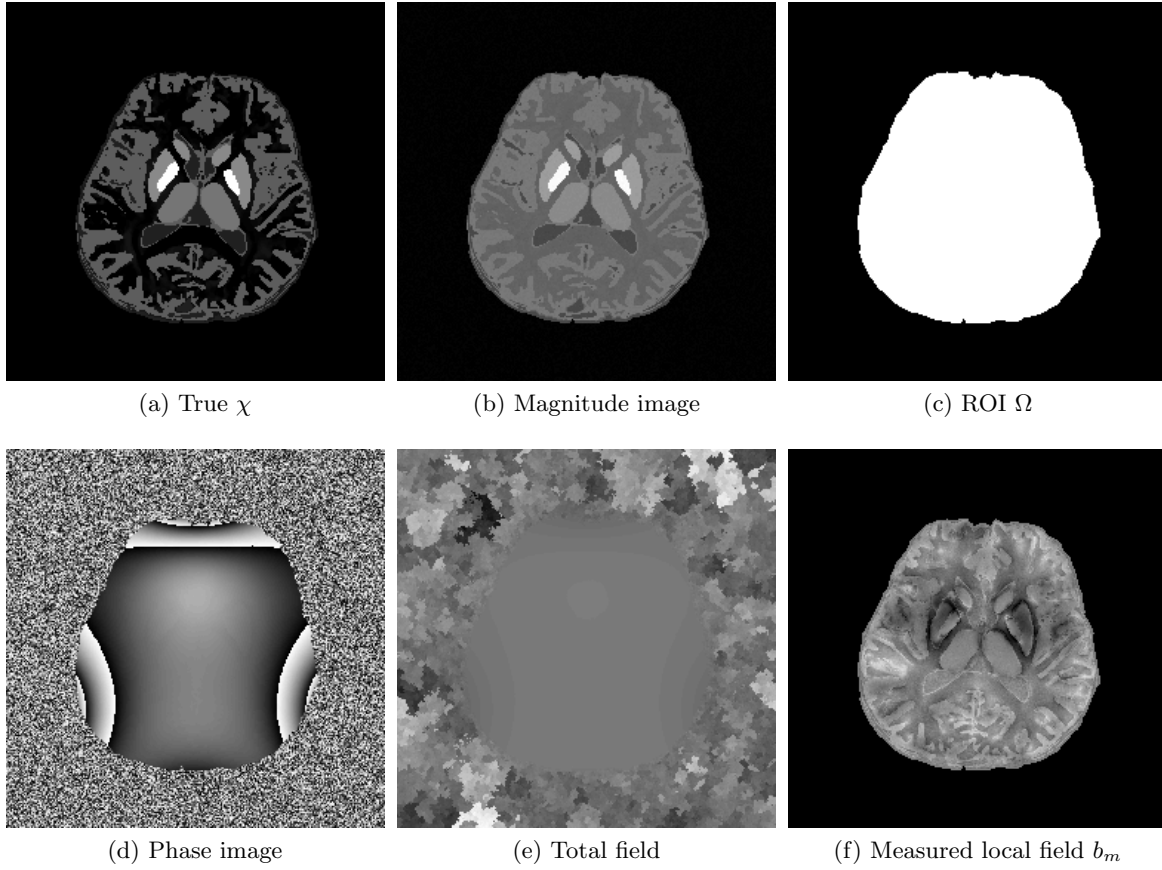


**Figure 5.** *Axial slice images of synthesized data sets for the brain phantom experiments.*



Table 1

Comparison of relative error, structural similarity index map, and high frequency error norm. The bold-faced numbers indicate the best result.

Indices	TKD (1.5)	Tikhonov (1.6)	Integral (2.20)	Differential (2.21)	HIRE (2.18)
RMSE	0.5579	0.5546	0.5222	0.5763	<b>0.4123</b>
SSIM	0.6546	0.6474	0.7269	0.6443	<b>0.7479</b>
HFEN	0.3534	0.4719	0.3062	0.4611	<b>0.2759</b>

All regularization based models (2.18), (2.20), and (2.21) are initialized with  $\chi^0 = 0$ , and we also initialize the HIRE model (2.18) with  $v^0 = 0$ . For the parameters, we choose  $\hbar = 0.125$  for (1.5),  $\varepsilon = 0.1$  for (1.6),  $\nu = 0.00025$  for (2.20),  $\nu = 0.002$  for (2.21), and  $\nu = 0.00025$  and  $\lambda = 0.00125$  for (2.18). In addition, we choose  $\beta = 0.05$  for all split Bregman algorithms to solve the regularization based models including Algorithm 1.

Table 1 summarizes the relative error, the SSIM, and the HFEN of the aforementioned five restoration models, and Figures 6 and 7 present visual comparisons of the results. We can see that the proposed HIRE model (2.18) consistently outperforms both the direct methods ((1.5) and (1.6)) and the single system regularization based approaches ((2.20) and (2.21)). At first glance, this verifies the convention that the regularization based models in general performs better in solving the ill-posed inverse problem of QSM than the direct methods [29, 56]. Most importantly, this result demonstrates that the measured local field data obtained from the phase of a complex GRE MR signal contains the harmonic incompatibility other than the noise, which agrees with our theoretical discovery. Compared to the integral approach (2.20) and the differential approach (2.21), we can see that the HIRE model (2.18) yields the best reconstruction results, as shown in Figures 6f and 7f which agree with the improvements of the indices. This performance gain mainly comes from the fact the proposed HIRE model takes both the noise in the measured data and the harmonic incompatibility (the incompatibility other than the noise) at the same time. Meanwhile, this harmonic incompatibility is not taken into account in the integral approach (2.20). As a consequence, the reconstructed susceptibility image contains the shadow artifacts as shown in Figures 6d and 7d, even though the streaking artifacts are effectively suppressed. In addition, the differential approach (2.21) can remove the harmonic incompatibility in the measured data in advance, and leads to the shadow artifact removal. However, since the noise in  $b_m$  was amplified by the discrete Laplacian  $\mathcal{L}$ , the final reconstructed image suffers from the artifacts due to the noise as shown in Figures 6e and 7e, leading to the degradation in indices at the same time. Hence, the reconstructed image from the proposed HIRE model has the overall best quality in both the indices and the visual quality.

**3.2. Experiments on In Vivo MR Data.** The in vivo MR data experiments are conducted using  $256 \times 256 \times 146$  image with spatial resolution  $0.9375 \times 0.9375 \times 1\text{mm}^3$  which can be downloaded on Cornell MRI Research Lab webpage. Using the wrapped phase image presented in Figures 8c and 9c, we unwrap the phase using the method in [22] to obtain the total field  $b$  in Figures 8d and 9d. Then the measured local field data  $b_m$  in Figures 8e and 9e is obtained by solving the Poisson's equation (2.10) using the method in [61].



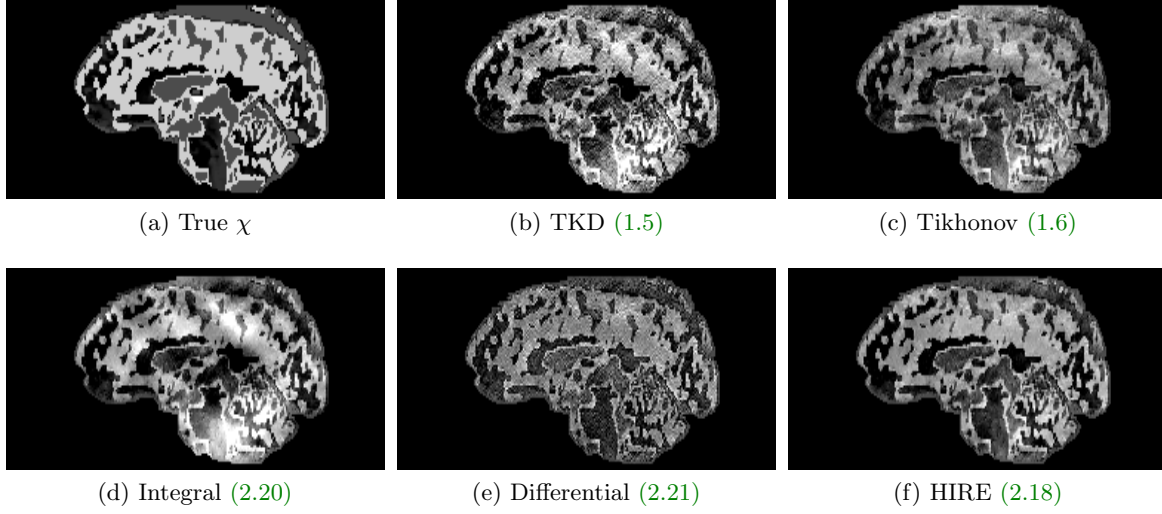


**Figure 6.** Sagittal slice images which compare QSM reconstruction methods for the brain phantom experiments. All sagittal slice images of brain phantom experimental results are displayed in the window level  $[-0.03, 0.07]$  for the fair comparison.

As in subsection 3.1, the models (2.18), (2.20), and (2.21) are initialized with  $\chi^0 = 0$ , and we further initialize the HIRE model (2.18) with  $v^0 = 0$ . For the parameters, we choose  $\hbar = 0.1$  for (1.5),  $\varepsilon = 0.1$  for (1.6),  $\nu = 0.0005$  for (2.20),  $\nu = 0.005$  for (2.21), and  $\nu = 0.00025$  and  $\lambda = 0.00125$  for (2.18) respectively. Finally, the parameter  $\beta$  in the split Bregman algorithm is chosen to be the same as the brain phantom experiments.

Figures 10 and 11 display the visual comparisons of the reconstruction results, and the zoom-in views of Figure 10 are provided in Figures 12 and 13. Since the reference image is not available for in vivo MR data, it is in general more difficult to provide quantitative evaluations than the numerical brain phantom. Nonetheless, we can see from the viewpoint of visual comparison that the pros and cons of the reconstruction methods are almost the same as the numerical brain phantom experiments. It is also worth noting that the proposed HIRE model can reduce the streaking artifacts which propagate from  $\partial\Omega$  into  $\Omega$  as well as the shadow artifacts. As pointed out in [57], the in vivo local field data is prone to the outliers near  $\partial\Omega$  because the GRE signal lacks information outside  $\Omega$ . Hence, we can see that most streaking artifacts propagate from these outliers near  $\partial\Omega$  into the ROI. However, thanks to the sparsity promoting property of  $\ell_1$  norm, the term  $\lambda \|\mathcal{L}v\|_1$  in (2.18) can somehow capture and remove them, leading to the suppression of artifacts propagating from  $\partial\Omega$  into  $\Omega$  as well. Finally, even though we can also note that the Tikhonov regularization can somehow reduce the artifacts as shown in Figures 12b and 13b, there are some losses of features compared to the HIRE model in Figures 12e and 13e, due to the smoothness prior of the susceptibility image. Hence, the proposed HIRE model has the best overall performance in terms of the artifact suppression and the feature preservation.

**4. Conclusion.** In this paper, we proposed a new regularization based susceptibility reconstruction model. The proposed HIRE model is based on the identification of the harmonic

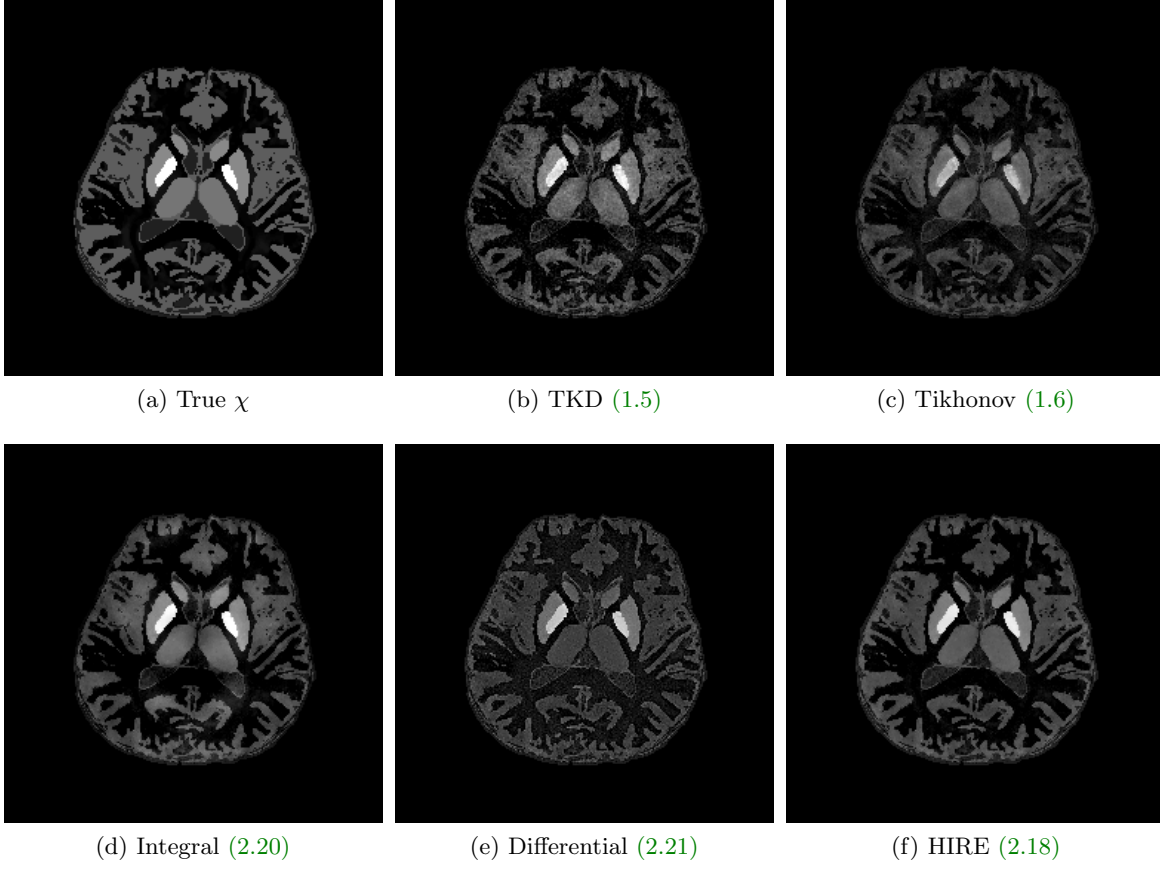


**Figure 7.** Axial slice images which compare QSM reconstruction methods for the brain phantom experiments. All axial slice images of brain phantom experimental results are displayed in the window level  $[-0.03, 0.19]$  for the fair comparison.

incompatibility in the measured local field data arising from the underlying PDE (1.8). The harmonic property is imposed as a prior of incompatibility via the sparsity under the Laplacian into the integral approach so that we can apply the idea of two system regularization model. By doing so, we can take the incompatibility in the data which is other than the additive noise into account, achieving the susceptibility image reconstruction with less artifacts. Finally, the experimental results show that our proposed approach (2.18) outperforms the existing approaches in both brain phantom and in vivo MR data.

**Appendix A. Preliminaries on Wavelet Frames.** Provided here is a brief introduction on the tight wavelet frames. Interested readers may consult [13, 14, 43] for theories of frames and wavelet frames, [50] for a short survey on the theory and applications of frames, and [18, 19] for more detailed surveys.

For a given  $\Psi = \{\psi_1, \dots, \psi_r\} \subseteq L_2(\mathbb{R}^d)$  with  $d \in \mathbb{N}$ , a quasi-affine system  $\mathcal{X}(\Psi)$  generated

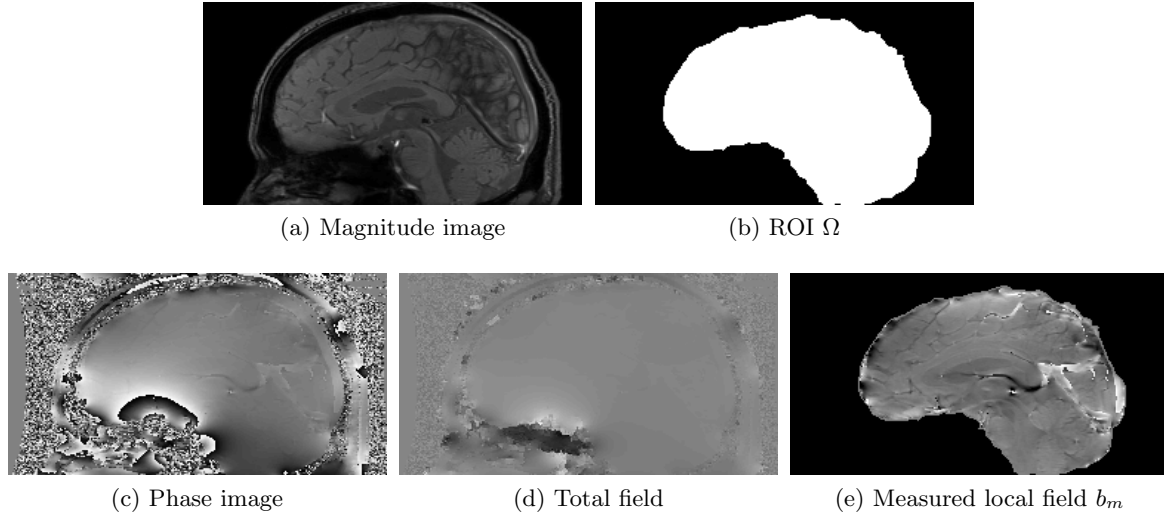


**Figure 8.** *Sagittal slice images of data sets for the in vivo MR data experiments.*

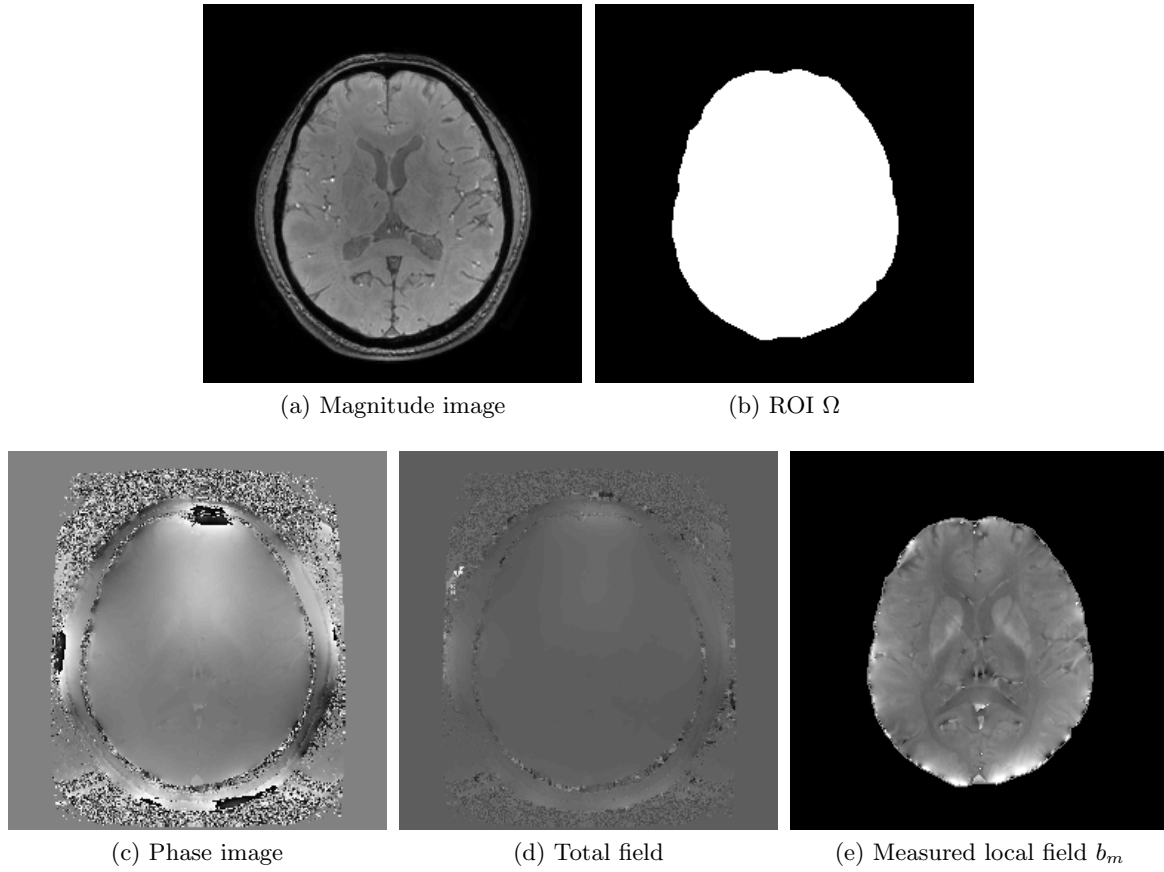


**Figure 9.** *Axial slice images of data sets for the in vivo MR data experiments.*

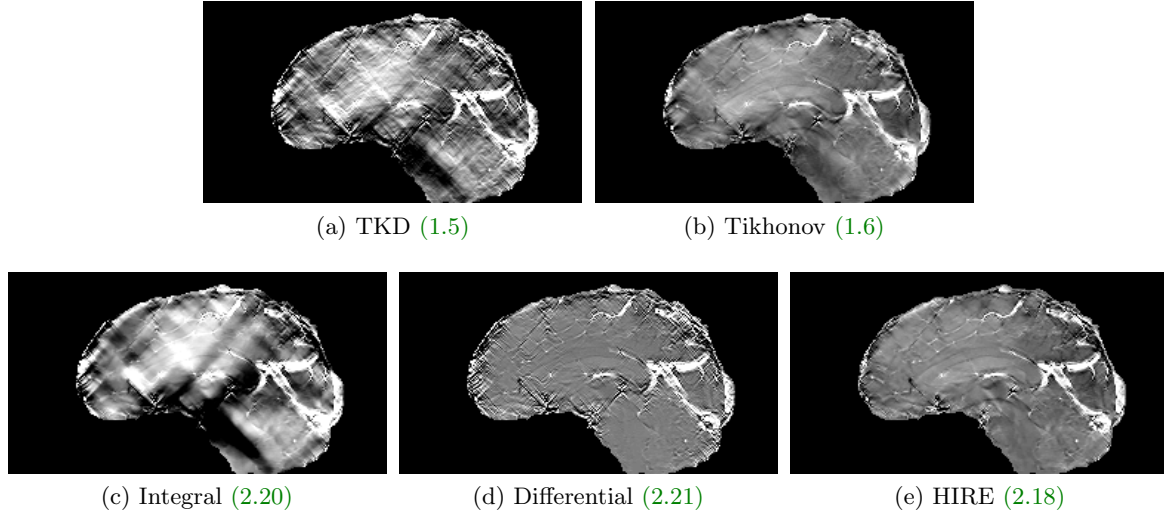


**Figure 10.** Sagittal slice images which compare QSM reconstruction methods for the *in vivo* MR data experiments. All images of *in vivo* MR data experimental results are displayed in the window level  $[-0.2, 0.2]$  for the fair comparison.

by  $\Psi$  is the collection of the dilations and the shifts of the elements in  $\Psi$ :

$$\mathcal{X}(\Psi) = \left\{ \psi_{\alpha, n, \mathbf{k}} : 1 \leq \alpha \leq r, n \in \mathbb{Z}, \mathbf{k} \in \mathbb{Z}^d \right\}, \quad (\text{A.1})$$

where  $\psi_{\alpha, n, \mathbf{k}}$  is defined as

$$\psi_{\alpha, n, \mathbf{k}} = \begin{cases} 2^{\frac{nd}{2}} \psi_{\alpha}(2^n \cdot -\mathbf{k}) & n \geq 0; \\ 2^{nd} \psi_{\alpha}(2^n \cdot -2^n \mathbf{k}) & n < 0. \end{cases} \quad (\text{A.2})$$

We say that  $\mathcal{X}(\Psi)$  is a tight wavelet frame on  $L_2(\mathbb{R}^d)$  if we have

$$\|f\|_{L_2(\mathbb{R}^d)}^2 = \sum_{\alpha=1}^r \sum_{n \in \mathbb{Z}} \sum_{\mathbf{k} \in \mathbb{Z}^d} |\langle f, \psi_{\alpha, n, \mathbf{k}} \rangle|^2 \quad (\text{A.3})$$

for every  $f \in L_2(\mathbb{R}^d)$ . In this case, each  $\psi_{\alpha}$  is called a (tight) framelet, and  $\langle f, \psi_{\alpha, n, \mathbf{k}} \rangle$  is called the canonical coefficient of  $f$ .

The constructions of (anti-)symmetric and compactly supported framelets  $\Psi$  are usually based on a multiresolution analysis (MRA); we first find some compactly supported refinable function  $\phi$  with a refinement mask  $q_0$  such that

$$\phi = 2^d \sum_{\mathbf{k} \in \mathbb{Z}^d} q_0[\mathbf{k}] \phi(2 \cdot -\mathbf{k}). \quad (\text{A.4})$$

Then the MRA based construction of  $\Psi = \{\psi_1, \dots, \psi_r\} \subseteq L_2(\mathbb{R}^d)$  is to find finitely supported masks  $q_{\alpha}$  such that

$$\psi_{\alpha} = 2^d \sum_{\mathbf{k} \in \mathbb{Z}^d} q_{\alpha}[\mathbf{k}] \phi(2 \cdot -\mathbf{k}), \quad \alpha = 1, \dots, r. \quad (\text{A.5})$$

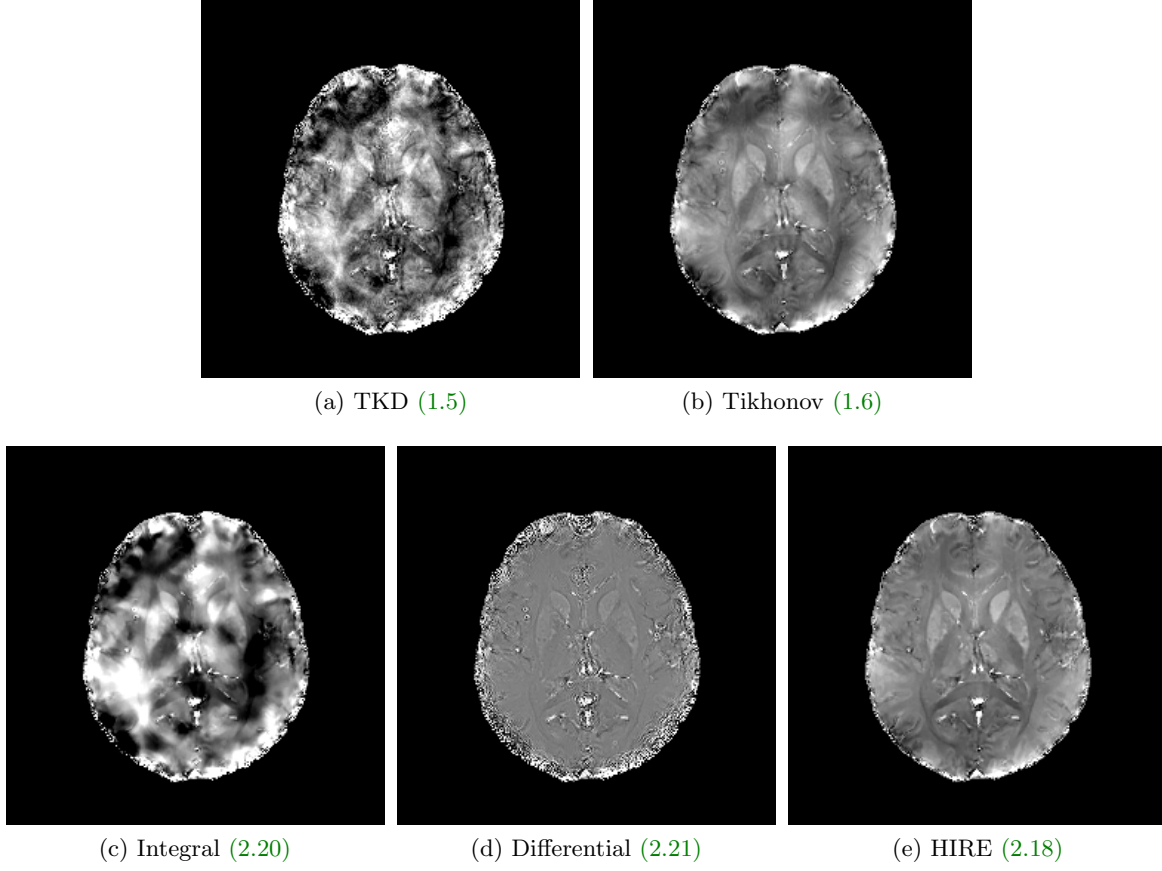


**Figure 11.** Axial slice images which compare QSM reconstruction methods for the *in vivo* MR data experiments.

The sequences  $q_1, \dots, q_r$  are called wavelet frame mask or the high pass filters of the system, and the refinement mask  $q_0$  is also called the low pass filter.

The unitary extension principle (UEP) of [43] provides a general theory of the construction of MRA based tight wavelet frames. Briefly speaking, as long as  $\{q_0, q_1, \dots, q_r\}$  are compactly supported and their Fourier series

$$\hat{q}_\alpha(\boldsymbol{\xi}) = \sum_{\mathbf{k} \in \mathbb{Z}^d} q_\alpha[\mathbf{k}] e^{-i\boldsymbol{\xi} \cdot \mathbf{k}}, \quad \alpha = 0, \dots, r, \quad \boldsymbol{\xi} \in \mathbb{R}^d$$

satisfy

$$\sum_{\alpha=0}^r |\hat{q}_\alpha(\boldsymbol{\xi})|^2 = 1 \quad \text{and} \quad \sum_{\alpha=0}^r \hat{q}_\alpha(\boldsymbol{\xi}) \overline{\hat{q}_\alpha(\boldsymbol{\xi} + \boldsymbol{\nu})} = 0 \quad (\text{A.6})$$

for all  $\boldsymbol{\nu} \in \{0, \pi\}^d \setminus \{\mathbf{0}\}$  and  $\boldsymbol{\xi} \in [-\pi, \pi]^d$ , the quasi-affine system  $\mathcal{X}(\boldsymbol{\Psi})$  with  $\boldsymbol{\Psi} = \{\psi_1, \dots, \psi_r\}$  defined by (A.5) forms a tight frame of  $L_2(\mathbb{R}^d)$ , and the filters  $\{q_0, q_1, \dots, q_r\}$  form a discrete tight frame on  $\ell_2(\mathbb{Z}^d)$  [18].

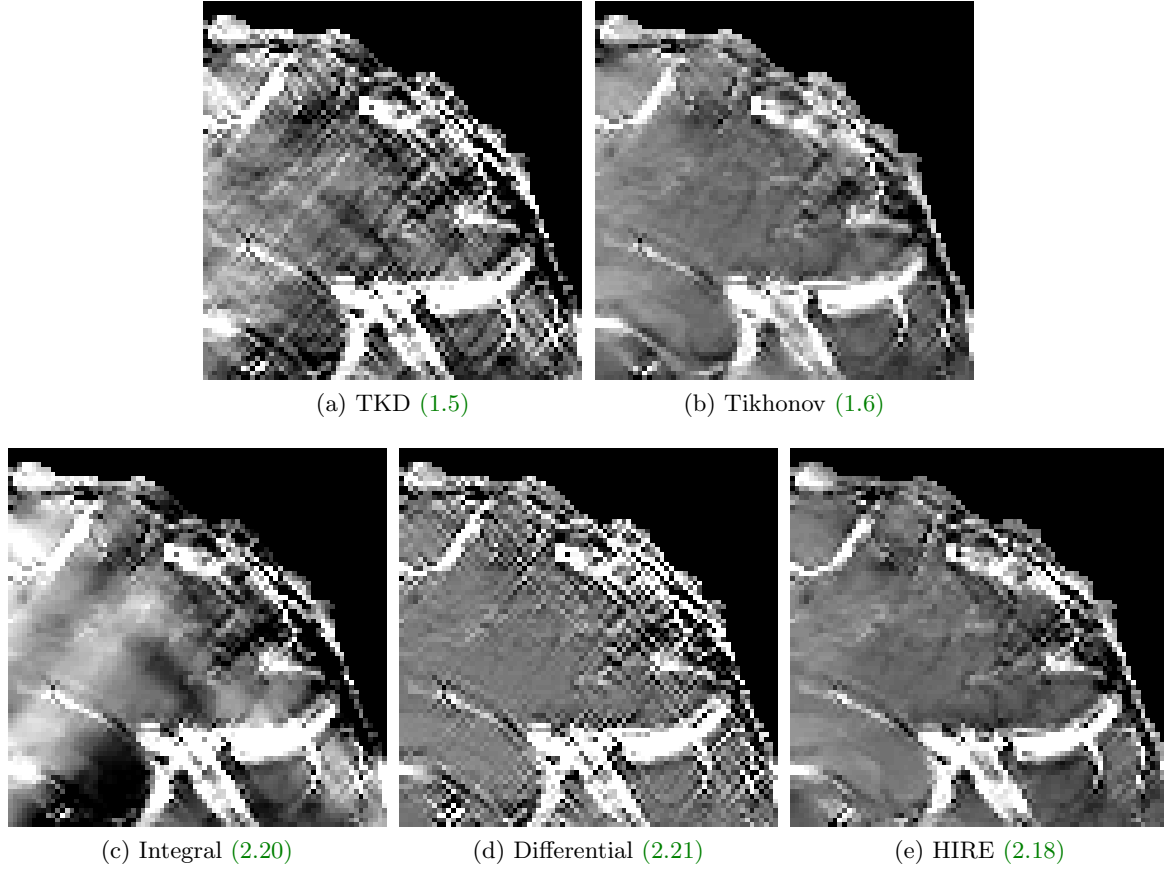


**Figure 12.** Zoom-in views of *Figure 10*.

The tight frame on  $L_2(\mathbb{R}^d)$  with  $d \geq 2$  can be constructed by taking tensor products of univariate tight framelets [6, 7, 13, 18]. Given a set of univariate masks  $\{q_0, q_1, \dots, q_r\}$ , we define multivariate masks  $q_\alpha[\mathbf{k}]$  with  $\alpha = (\alpha_1, \dots, \alpha_d)$  and  $\mathbf{k} = (k_1, \dots, k_d) \in \mathbb{Z}^d$  as

$$q_\alpha[\mathbf{k}] = q_{\alpha_1}[k_1] \cdots q_{\alpha_d}[k_d], \quad 0 \leq \alpha_1, \dots, \alpha_d \leq r, \quad \mathbf{k} = (k_1, \dots, k_d) \in \mathbb{Z}^d.$$

The corresponding multivariate refinable function and framelets are defined as

$$\psi_\alpha(\mathbf{x}) = \psi_{\alpha_1}(x_1) \cdots \psi_{\alpha_d}(x_d), \quad 0 \leq \alpha_1, \dots, \alpha_d \leq r, \quad \mathbf{x} = (x_1, \dots, x_d) \in \mathbb{R}^d$$

with  $\psi_0 = \phi$  for convenience. If the univariate masks  $\{q_\alpha\}$  are constructed from UEP, then we can verify that  $\{q_\alpha\}$  satisfies (A.6) and thus  $\mathcal{X}(\Psi)$  with  $\Psi = \{\psi_\alpha : \alpha \in \{0, \dots, r\}^d \setminus \{\mathbf{0}\}\}$  forms a tight frame for  $L_2(\mathbb{R}^d)$ .

In the discrete setting, let  $\mathcal{I}_d \simeq \mathbb{R}^{N_1 \times \dots \times N_d}$  be the space of real valued functions defined on a regular grid  $\{0, 1, \dots, N_1 - 1\} \times \dots \times \{0, 1, \dots, N_d - 1\}$ . The fast framelet decomposition, or the analysis operator with  $L$  levels of decomposition is defined as

$$Wu = \{W_{l,\alpha}u : (l, \alpha) \in (\{0, \dots, L-1\} \times \mathbb{B}) \cup \{(L-1, \mathbf{0})\}\} \quad (\text{A.7})$$

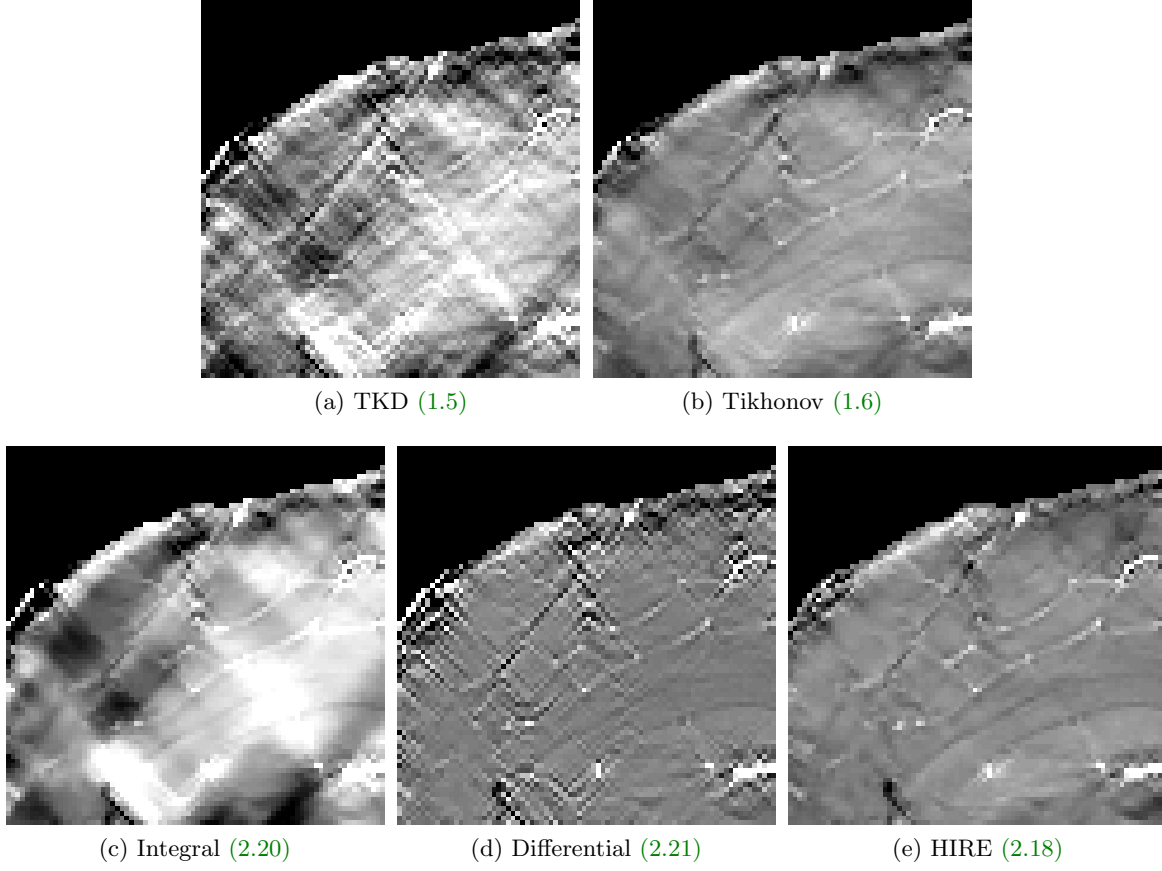


**Figure 13.** Another zoom-in views of *Figure 10*.

where  $\mathbb{B} = \{0, \dots, r\}^d \setminus \{\mathbf{0}\}$  is the framelet band. Then the frame coefficients  $W_{l,\alpha}u \in \mathcal{I}_d$  of  $u \in \mathcal{I}_d$  at level  $l$  and band  $\alpha$  are defined as

$$W_{l,\alpha}u = q_{l,\alpha}[-\cdot] \circledast u.$$

where  $\circledast$  denotes the discrete convolution with a certain boundary condition (e.g. the periodic boundary condition), and  $q_{l,\alpha}$  is defined as

$$q_{l,\alpha} = \tilde{q}_{l,\alpha} \circledast \tilde{q}_{l-1,\mathbf{0}} \circledast \dots \circledast \tilde{q}_{0,\mathbf{0}} \quad \text{with} \quad \tilde{q}_{l,\alpha}[\mathbf{k}] = \begin{cases} q_{\alpha}[2^{-l}\mathbf{k}], & \mathbf{k} \in 2^l\mathbb{Z}^d; \\ 0, & \mathbf{k} \notin 2^l\mathbb{Z}^d. \end{cases} \quad (\text{A.8})$$

We denote by  $W^T$ , the adjoint of  $W$ , the fast reconstruction (or the synthesis operator). Then by UEP (A.6), we have  $W^TW = I$ .

**Acknowledgments.** We would like thank the authors in [57, 59] for making the data sets and the MATLAB toolbox available so that the experiments can be implemented.

## REFERENCES



- [1] J. ACOSTA-CABRONERO, G. B. WILLIAMS, A. CARDENAS-BLANCO, R. J. ARNOLD, V. LUPSON, AND P. J. NESTOR, *In Vivo Quantitative Susceptibility Mapping (QSM) in Alzheimer's Disease*, PloS one, 8 (2013), p. e81093, <https://doi.org/10.1371/journal.pone.0081093>.
- [2] L. BAO, X. LI, C. CAI, Z. CHEN, AND P. C. M. VAN ZIJL, *Quantitative Susceptibility Mapping Using Structural Feature Based Collaborative Reconstruction (SFCR) in the Human Brain*, IEEE Trans. Med. Imag., 35 (2016), pp. 2040–2050, <https://doi.org/10.1109/TMI.2016.2544958>.
- [3] K. BREDIES AND M. HOLLER, *Regularization of Linear Inverse Problems with Total Generalized Variation*, J. Inverse Ill-Posed Probl., 22 (2014), pp. 871–913, <https://doi.org/10.1515/jip-2013-0068>.
- [4] K. BREDIES, K. KUNISCH, AND T. POCK, *Total Generalized Variation*, SIAM J. Imaging Sci., 3 (2010), pp. 492–526, <https://doi.org/10.1137/090769521>.
- [5] J. F. CAI, R. H. CHAN, AND Z. SHEN, *Simultaneous Cartoon and Texture Inpainting*, Inverse Probl. Imaging, 4 (2010), pp. 379–395, <https://doi.org/10.3934/ipi.2010.4.379>.
- [6] J. F. CAI, B. DONG, S. OSHER, AND Z. SHEN, *Image Restoration: Total Variation, Wavelet Frames, and Beyond*, J. Amer. Math. Soc., 25 (2012), pp. 1033–1089, <https://doi.org/10.1090/S0894-0347-2012-00740-1>.
- [7] J. F. CAI, B. DONG, AND Z. SHEN, *Image Restoration: a Wavelet Frame Based Model for Piecewise Smooth Functions and Beyond*, Appl. Comput. Harmon. Anal., 41 (2016), pp. 94–138, <https://doi.org/10.1016/j.acha.2015.06.009>.
- [8] J. F. CAI, S. OSHER, AND Z. SHEN, *Split Bregman Methods and Frame Based Image Restoration*, Multiscale Model. Simul., 8 (2009/10), pp. 337–369, <https://doi.org/10.1137/090753504>.
- [9] A. CHAI AND Z. SHEN, *Deconvolution: a Wavelet Frame Approach*, Numer. Math., 106 (2007), pp. 529–587, <https://doi.org/10.1007/s00211-007-0075-0>.
- [10] W. CHEN, S. A. GAUTHIER, A. GUPTA, J. COMUNALE, T. LIU, S. WANG, M. PEI, D. PITT, AND Y. WANG, *Quantitative Susceptibility Mapping of Multiple Sclerosis Lesions at Various Ages*, Radiology, 271 (2014), pp. 183–192, <https://doi.org/10.1148/radiol.13130353>, <https://arxiv.org/abs/https://doi.org/10.1148/radiol.13130353>. PMID: 24475808.
- [11] Z. CHEN AND V. D. CALHOUN, *Computed Inverse Resonance Imaging for Magnetic Susceptibility Map Reconstruction*, J. Comput. Assist. Tomogr., 36 (2012), pp. 265–274, <https://doi.org/10.1097/rct.0b013e3182455cab>.
- [12] J. K. CHOI, H. S. PARK, S. WANG, Y. WANG, AND J. K. SEO, *Inverse Problem in Quantitative Susceptibility Mapping*, SIAM J. Imaging Sci., 7 (2014), pp. 1669–1689, <https://doi.org/10.1137/140957433>.
- [13] I. DAUBECHIES, *Ten Lectures on Wavelets*, vol. 61 of CBMS-NSF Regional Conference Series in Applied Mathematics, Society for Industrial and Applied Mathematics (SIAM), Philadelphia, PA, 1992, <https://doi.org/10.1137/1.9781611970104>.
- [14] I. DAUBECHIES, B. HAN, A. RON, AND Z. SHEN, *Framelets: MRA-Based Constructions of Wavelet Frames*, Appl. Comput. Harmon. Anal., 14 (2003), pp. 1–46, [https://doi.org/10.1016/S1063-5203\(02\)00511-0](https://doi.org/10.1016/S1063-5203(02)00511-0).
- [15] L. DE ROCHEFORT, R. BROWN, M. R. PRINCE, AND Y. WANG, *Quantitative MR Susceptibility Mapping Using Piece-Wise Constant Regularized Inversion of the Magnetic Field*, Magn. Reson. Med., 60 (2008), pp. 1003–1009, <https://doi.org/10.1002/mrm.21710>.
- [16] A. V. DIMOV, Z. LIU, P. SPINCEMAILLE, M. R. PRINCE, J. DU, AND Y. WANG, *Bone Quantitative Susceptibility Mapping Using a Chemical Species-Specific  $R2^*$  Signal Model with Ultrashort and Conventional Echo Data*, Magn. Reson. Med., 79 (2018), pp. 121–128, <https://doi.org/10.1002/mrm.26648>.
- [17] B. DONG, H. JI, J. LI, Z. SHEN, AND Y. XU, *Wavelet Frame Based Blind Image Inpainting*, Appl. Comput. Harmon. Anal., 32 (2012), pp. 268–279, <https://doi.org/10.1016/j.acha.2011.06.001>.
- [18] B. DONG AND Z. SHEN, *MRA-Based Wavelet Frames and Applications*, in Mathematics in Image Processing, vol. 19 of IAS/Park City Math. Ser., Amer. Math. Soc., Providence, RI, 2013, pp. 9–158.
- [19] B. DONG AND Z. SHEN, *Image Restoration: A Data-Driven Perspective*, in Proceedings of the 8th International Congress on Industrial and Applied Mathematics, Higher Ed. Press, Beijing, 2015, pp. 65–108.
- [20] J. ECKSTEIN AND D. P. BERTSEKAS, *On the Douglas-Rachford Splitting Method and the Proximal Point Algorithm for Maximal Monotone Operators*, Math. Programming, 55 (1992), pp. 293–318, <https://doi.org/10.1007/BF01581204>.
- [21] L. C. EVANS, *Partial differential equations*, vol. 19 of Graduate Studies in Mathematics, American Mathematical Society, Providence, RI, second ed., 2010, <https://doi.org/10.1090/gsm/019>.

- [22] D. C. GHIGLIA AND M. D. PRITT, *Two-Dimensional Phase Unwrapping: Theory, Algorithms, and Software*, Wiley-Interscience publication, Wiley, 1998.
- [23] T. GOLDSTEIN AND S. J. OSHER, *The Split Bregman Method for L1-Regularized Problems*, SIAM J. Imaging Sci., 2 (2009), pp. 323–343, <https://doi.org/10.1137/080725891>.
- [24] E. M. HAACKE, R. W. BROWN, M. R. THOMPSON, AND R. VENKATESAN, *Magnetic Resonance Imaging : Physical Principles and Sequence Design*, Wiley, 1st ed., June 1999.
- [25] E. M. HAACKE, S. LIU, S. BUCH, W. ZHENG, D. WU, AND Y. YE, *Quantitative Susceptibility Mapping: Current Status and Future Directions*, Magn. Reson. Imaging, 33 (2015), pp. 1 – 25, <https://doi.org/10.1016/j.mri.2014.09.004>.
- [26] E. M. HAACKE, J. TANG, J. NEELAVALLI, AND Y. C. N. CHENG, *Susceptibility Mapping as a Means to Visualize Veins and Quantify Oxygen Saturation*, J. Magn. Reson. Imag., 32 (2010), pp. 663–676, <https://doi.org/10.1002/jmri.22276>.
- [27] H. JI AND K. WANG, *Robust Image Deblurring With an Inaccurate Blur Kernel*, IEEE Trans. Image Process., 21 (2012), pp. 1624–1634, <https://doi.org/10.1109/TIP.2011.2171699>.
- [28] Y. KEE, J. CHO, K. DEH, Z. LIU, P. SPINCEMAILLE, AND Y. WANG, *Coherence Enhancement in Quantitative Susceptibility Mapping by Means of Anisotropic Weighting in Morphology Enabled Dipole Inversion*, Magn. Reson. Med., 79 (2018), pp. 1172–1180, <https://doi.org/10.1002/mrm.26748>.
- [29] Y. KEE, Z. LIU, L. ZHOU, A. DIMOV, J. CHO, L. DE ROCHEFORT, J. K. SEO, AND Y. WANG, *Quantitative Susceptibility Mapping (QSM) Algorithms: Mathematical Rationale and Computational Implementations*, IEEE Trans. Biomed. Eng., 64 (2017), pp. 2531–2545, <https://doi.org/10.1109/TBME.2017.2749298>.
- [30] J. KLOHS, A. DEISTUNG, F. SCHWESER, J. GRANDJEAN, M. DOMINIETTO, C. WASCHKIES, R. M. NITSCH, I. KNUESEL, J. R. REICHENBACH, AND M. RUDIN, *Detection of Cerebral Microbleeds with Quantitative Susceptibility Mapping in the Arcabeta Mouse Model of Cerebral Amyloidosis*, J. Cerebr. Blood F. Met., 31 (2011), pp. 2282–2292, <https://doi.org/10.1038/jcbfm.2011.118>, <https://arxiv.org/abs/https://doi.org/10.1038/jcbfm.2011.118>. PMID: 21847134.
- [31] B. KRESSLER, L. DE ROCHEFORT, T. LIU, P. SPINCEMAILLE, J. QUAN, AND Y. WANG, *Nonlinear Regularization for Per Voxel Estimation of Magnetic Susceptibility Distributions From MRI Field Maps*, IEEE Trans. Med. Imag., 29 (2010), pp. 273–281, <https://doi.org/10.1109/TMI.2009.2023787>.
- [32] C. LANGKAMMER, K. BREDIES, B. A. POSER, M. BARTH, G. REISHOFER, A. P. FAN, B. BILGIC, F. FAZEKAS, C. MAINERO, AND S. ROPELE, *Fast Quantitative Susceptibility Mapping Using 3D EPI and Total Generalized Variation*, NeuroImage, 111 (2015), pp. 622 – 630, <https://doi.org/https://doi.org/10.1016/j.neuroimage.2015.02.041>.
- [33] J. LI, C. MIAO, Z. SHEN, G. WANG, AND H. YU, *Robust Frame Based X-ray CT Reconstruction*, J. Comput. Math., 34 (2016), pp. 683–704, <https://doi.org/10.4208/jcm.1608-m2016-0499>.
- [34] W. LI, A. V. AVRAM, B. WU, X. XIAO, AND C. LIU, *Integrated Laplacian-Based Phase Unwrapping and Background Phase Removal for Quantitative Susceptibility Mapping*, NMR in Biomedicine, 27 (2014), pp. 219–227, <https://doi.org/10.1002/nbm.3056>. NBM-13-0182.R2.
- [35] T. LIU, I. KHALIDOV, L. DE ROCHEFORT, P. SPINCEMAILLE, J. LIU, A. J. TSIOURIS, AND Y. WANG, *A Novel Background Field Removal Method for MRI Using Projection onto Dipole Fields (PDF)*, NMR Biomed, 24 (2011), pp. 1129–1136, <https://doi.org/10.1002/nbm.1670>.
- [36] T. LIU, J. LIU, L. DE ROCHEFORT, P. SPINCEMAILLE, I. KHALIDOV, J. R. LEDOUX, AND Y. WANG, *Morphology Enabled Dipole Inversion (MEDI) from a Single-Angle Acquisition: Comparison with COSMOS in Human Brain Imaging*, Magn. Reson. Med., 66 (2011), pp. 777–783, <https://doi.org/10.1002/mrm.22816>.
- [37] T. LIU, P. SPINCEMAILLE, L. DE ROCHEFORT, B. KRESSLER, AND Y. WANG, *Calculation of Susceptibility through Multiple Orientation Sampling (COSMOS): A Method for Conditioning the Inverse Problem from Measured Magnetic Field Map to Susceptibility Source Image in MRI*, Magn. Reson. Med., 61 (2009), pp. 196–204, <https://doi.org/10.1002/mrm.21828>.
- [38] T. LIU, P. SPINCEMAILLE, L. DE ROCHEFORT, R. WONG, M. PRINCE, AND Y. WANG, *Unambiguous Identification of Superparamagnetic Iron Oxide Particles through Quantitative Susceptibility Mapping of the Nonlinear Response to Magnetic Fields*, Magn. Reson. Imaging, 28 (2010), pp. 1383 – 1389, <https://doi.org/https://doi.org/10.1016/j.mri.2010.06.011>.
- [39] T. LIU, C. WISNIEFF, M. LOU, W. CHEN, P. SPINCEMAILLE, AND Y. WANG, *Nonlinear Formulation*

- of the Magnetic Field to Source Relationship for Robust Quantitative Susceptibility Mapping, *Magn. Reson. Med.*, 69 (2013), pp. 467–476, <https://doi.org/10.1002/mrm.24272>.
- [40] F. NATTERER, *Image Reconstruction in Quantitative Susceptibility Mapping*, *SIAM J. Imaging Sci.*, 9 (2016), pp. 1127–1131, <https://doi.org/10.1137/16M1064878>.
- [41] B. PALACIOS, G. UHLMANN, AND Y. WANG, *Reducing Streaking Artifacts in Quantitative Susceptibility Mapping*, *SIAM J. Imaging Sci.*, 10 (2017), pp. 1921–1934, <https://doi.org/10.1137/16M1096475>.
- [42] S. RAVISHANKAR AND Y. BRESLER, *MR Image Reconstruction From Highly Undersampled  $k$ -Space Data by Dictionary Learning*, *IEEE Trans. Med. Imag.*, 30 (2011), pp. 1028–1041, <https://doi.org/10.1109/TMI.2010.2090538>.
- [43] A. RON AND Z. SHEN, *Affine Systems in  $L_2(\mathbf{R}^d)$ : the Analysis of the Analysis Operator*, *J. Funct. Anal.*, 148 (1997), pp. 408–447, <https://doi.org/10.1006/jfan.1996.3079>.
- [44] L. I. RUDIN, S. OSHER, AND E. FATEMI, *Nonlinear Total Variation Based Noise Removal Algorithms*, *Phys. D*, 60 (1992), pp. 259–268. *Experimental mathematics: computational issues in nonlinear science* (Los Alamos, NM, 1991).
- [45] F. SCHWESER, A. DEISTUNG, B. W. LEHR, AND J. R. REICHENBACH, *Differentiation between Diamagnetic and Paramagnetic Cerebral Lesions based on Magnetic Susceptibility Mapping*, *Med. Phys.*, 37 (2010), pp. 5165–5178, <https://doi.org/10.1118/1.3481505>.
- [46] F. SCHWESER, A. DEISTUNG, AND J. R. REICHENBACH, *Foundations of MRI Phase Imaging and Processing for Quantitative Susceptibility Mapping (QSM)*, *Zeitschrift für Medizinische Physik*, 26 (2016), pp. 6 – 34, <https://doi.org/https://doi.org/10.1016/j.zemedi.2015.10.002>.
- [47] F. SCHWESER, K. SOMMER, A. DEISTUNG, AND J. R. REICHENBACH, *Quantitative Susceptibility Mapping for Investigating Subtle Susceptibility Variations in the Human Brain*, *NeuroImage*, 62 (2012), pp. 2083–2100, <https://doi.org/http://dx.doi.org/10.1016/j.neuroimage.2012.05.067>.
- [48] J. K. SEO AND E. J. WOO, *Nonlinear Inverse Problems in Imaging*, Wiley, 2012.
- [49] J. K. SEO, E. J. WOO, U. KATSCHER, AND Y. WANG, *Electro-Magnetic Tissue Properties MRI*, Imperial College Press, London, 1st ed., 2014.
- [50] Z. SHEN, *Wavelet Frames and Image Restorations*, in *Proceedings of the International Congress of Mathematicians. Volume IV*, Hindustan Book Agency, New Delhi, 2010, pp. 2834–2863.
- [51] K. SHMUELI, J. A. DE ZWART, P. VAN GELDEREN, T. LI, S. J. DODD, AND J. H. DUYN, *Magnetic Susceptibility Mapping of Brain Tissue In Vivo Using MRI Phase Data*, *Magn. Reson. Med.*, 62 (2009), pp. 1510–1522, <https://doi.org/10.1002/mrm.22135>.
- [52] S. M. SMITH, *Fast Robust Automated Brain Extraction*, *Human Brain Mapping*, 17 (2002), pp. 143–155, <https://doi.org/10.1002/hbm.10062>, <https://arxiv.org/abs/https://onlinelibrary.wiley.com/doi/pdf/10.1002/hbm.10062>.
- [53] E. M. STEIN AND R. SHAKARCHI, *Functional Analysis. Introduction to Further Topics in Analysis*, vol. 4 of *Princeton Lect. Anal.*, Princeton University Press, Princeton, NJ, 2011.
- [54] J. TANG, S. LIU, J. NEELAVALLI, Y. C. N. CHENG, S. BUCH, AND E. M. HAACKE, *Improving Susceptibility Mapping Using a Threshold-Based  $k$ -space/Image Domain Iterative Reconstruction Approach*, *Magn. Reson. Med.*, 69 (2013), pp. 1396–1407, <https://doi.org/10.1002/mrm.24384>.
- [55] J. M. G. VAN BERGEN, J. HUA, P. G. UNSCHULD, I. A. L. LIM, C. K. JONES, R. L. MARGOLIS, C. A. ROSS, P. C. M. VAN ZIJL, AND X. LI, *Quantitative Susceptibility Mapping Suggests Altered Brain Iron in Premanifest Huntington Disease*, *Amer. J. Neuroradiol.*, 37 (2016), pp. 789–796, <https://doi.org/10.3174/ajnr.A4617>, <https://arxiv.org/abs/http://www.ajnr.org/content/37/5/789.full.pdf>.
- [56] S. WANG, T. LIU, W. CHEN, P. SPINCEMAILLE, C. WISNIEFF, A. J. TSIOURIS, W. ZHU, C. PAN, L. ZHAO, AND Y. WANG, *Noise Effects in Various Quantitative Susceptibility Mapping Methods*, *IEEE Trans. Biomed. Eng.*, 60 (2013), pp. 3441–3448, <https://doi.org/10.1109/TBME.2013.2266795>.
- [57] Y. WANG AND T. LIU, *Quantitative Susceptibility Mapping (QSM): Decoding MRI Data for a Tissue Magnetic Biomarker*, *Magn. Reson. Med.*, 73 (2015), pp. 82–101, <https://doi.org/10.1002/mrm.25358>.
- [58] Z. WANG, A. C. BOVIK, H. R. SHEIKH, AND E. P. SIMONCELLI, *Image Quality Assessment: from Error Visibility to Structural Similarity*, *IEEE Trans. Image Process.*, 13 (2004), pp. 600–612, <https://doi.org/10.1109/TIP.2003.819861>.
- [59] C. WISNIEFF, T. LIU, P. SPINCEMAILLE, S. WANG, D. ZHOU, AND Y. WANG, *Magnetic Susceptibility Anisotropy: Cylindrical Symmetry from Macroscopically Ordered Anisotropic Molecules and Accuracy of MRI Measurements Using Few Orientations*, *NeuroImage*, 70 (2013), pp. 363 – 376, <https://doi.org/10.1016/j.neuroimage.2012.11.050>.

- [org/https://doi.org/10.1016/j.neuroimage.2012.12.050](https://doi.org/10.1016/j.neuroimage.2012.12.050).
- [60] B. WU, W. LI, A. GUIDON, AND C. LIU, *Whole Brain Susceptibility Mapping Using Compressed Sensing*, *Magn. Reson. Med.*, 67 (2012), pp. 137–147, <https://doi.org/10.1002/mrm.23000>.
- [61] D. ZHOU, T. LIU, P. SPINCEMAILLE, AND Y. WANG, *Background Field Removal by Solving the Laplacian Boundary Value Problem*, *NMR in Biomedicine*, 27 (2014), pp. 312–319, <https://doi.org/10.1002/nbm.3064>. NBM-13-0115.R3.